Article

Taphonomy of a Mysticete Whale from the Lower Pliocene of the Coast of Cádiz (Spain)

Giulia Bosio [1,*], Ildefonso Bajo-Campos [2], Alberto Collareta [3], Sergio Ros-Montoya [4], Daniel de la Torre [5], Giovanni Coletti [1] and Giovanni Bianucci [3]

1   Dipartimento di Scienze dell'Ambiente e della Terra, Università degli Studi di Milano-Bicocca, 20126 Milano, Italy; giovanni.p.m.coletti@gmail.com
2   Sección de Paleontología, Museo de Alcalá De Guadaíra, Alcalá de Guadaíra, 41500 Sevilla, Spain; ildebajo@gmail.com
3   Dipartimento di Scienze della Terra, Università di Pisa, 56126 Pisa, Italy; alberto.collareta@unipi.it (A.C.); giovanni.bianucci@unipi.it (G.B.)
4   Departamento de Ecología y Geología, Facultad de Ciencias, Universidad de Málaga, 29010 Málaga, Spain; sergiorosm@uma.es
5   5 C/Carretera Nueva, 32C, La Rinconada, 41309 Sevilla, Spain; delatorre.martin.daniel@gmail.com
*   Correspondence: giulia.bosio.giulia@gmail.com

Abstract: A fossil mysticete was discovered along the southwestern coast of Spain, occurring in a block detached from the Neogene deposits exposed along a coastal cliff at the locality of Conil de la Frontera (Cádiz, Spain). These deposits range from Pliocene to Pleistocene in age and include shallow-marine, mixed carbonate–siliciclastic sediments, with the whale being found in occurrence of a stratigraphic unconformity marked by *Thalassinoides* burrows. $^{87}Sr/^{86}Sr$ analyses on oyster shells associated with the skeleton suggest an Early Pliocene age, in agreement with the age of the lowermost unit cropping out at the study site. The studied cetacean specimen consists of an articulated, almost complete balaenopteroid skeleton exposed in the field dorsal side up; being contained in an upside-down block, however, it is preserved in ventral disposition. Bones exhibit a low degree of preservation of the cortical bone tissue, which locally features shark bite marks and *Osedax* traces as well as abundant encrustations of barnacles and ostreids. Two shark teeth were also found near the skeleton. Bones have preserved their main histological features, even though they locally exhibit microcracks, dissolution, substitution by Fe oxides, and microborings. Sediment particles and late diagenetic cements fill the medullary cavities. We propose that the whale carcass experienced refloating before sinking to the seafloor and that the skeleton was probably exposed on the seafloor for some time before being eventually buried.

Keywords: cetacean; Balaenopteroidea; fossilization; biostratinomy; fossil diagenesis; bioencrustation; whale-fall; *Osedax*; fossil traces; bones

1. Introduction

The preservation of cetacean carcasses involves a complex interplay of biological, environmental, geological, and chemical factors. Understanding the taphonomic processes that occur from the time of death to the eventual fossilization of these marine giants is essential for understanding their preservation in the rock record and for reconstructing their evolutionary history and paleoecology (e.g., [1–5]). Cetacean taphonomy encompasses various stages, from the initial biostratinomic phases that start from the death of the organism (e.g., [6–8]) to the late diagenetic phases involving the fossilization processes and the recent exposure (e.g., [9,10]). Several studies have also focused on the whale-fall communities that develop exclusively around cetacean carcasses in both recent and past times (e.g., [4,11] and references therein). Factors such as scavenging by marine organisms, transport by marine waves and currents, deposition on the seafloor, bacterial activity,

encrustation, burial, sediment and bone diagenesis, and secondary mineral precipitation all contribute to the eventual fossil preservation (e.g., [12–18]). By macroscopically and microscopically examining the taphonomic signatures left on cetacean bones, we can gain insights into the circumstances surrounding the whale death, the environment it inhabited, and the taphonomic pathways leading to its fossilization. Regarding mysticetes, studies have focused not only on exceptionally preserved single fossil specimens (e.g., [19–22]) but also on larger datasets (e.g., [16,18,23–28]).

Although the fossil remains of marine vertebrates (e.g., fishes, crocodilians, sirenians, and pinnipeds) are abundant in the Spanish Neogene (e.g., [29–34]), only a few cetacean specimens have been formally described to date [35]. These are mostly scattered and limited to small cranial, vertebral, and appendicular remains referred to the suborder Mysticeti, although fairly complete specimens have also been reported occasionally. Findings ascribed to the suborder Odontoceti have been reported in both the Miocene [29,32,36–43] and Pliocene strata [44–46]. Equally, mysticete remains have been reported from both the Miocene [37,47–49] and Pliocene strata [20,46,50–54]. These cetacean fossil specimens are found from the Lower Miocene to Pliocene strata in different regions of Spain, spreading across Galicia, Asturias, the Balearic Islands (Menorca), Catalonia (Tarragona and Barcelona), and Andalusia (Huelva, Sevilla, Cádiz, and Almería). In the latter region, cetacean remains are particularly abundant in the Vera and Guadalquivir basins.

The Neogene marine deposits of the western zone of the Guadalquivir Basin are very rich in marine vertebrate remains from both the Miocene and Pliocene strata [55,56]. In particular, records of fossil odontocetes come from the Upper Miocene of Sevilla [32,42], the Upper Miocene of Huelva [42], and the Lower Pliocene of Cádiz [45]. Mysticetes have been reported from the Upper Miocene of Sevilla [49], the Lower Pliocene of Huelva [20,52,53], and the Lower Pliocene of Sevilla [50], even though some dating should be revised (I.B.-C., personal observation). Still, they are only cited within geological works of general scope (see Table 1). In the study area, in the province of Cádiz, it is worth noting the presence of a very well-preserved odontocete specimen from the Neogene of the El Manantial site, located in Rota. This specimen is currently stored at the Municipal Museum of El Puerto de Santa María [45].

**Table 1.** Findings of fossil mysticetes in the Guadalquivir Basin.

Formation/Period	Locality (Province)	Suborder, Family	Material	References
Tortonian	Burguillos (Seville)	Mysticeti	Neurocranium	Sendra and Bajo 2013a [49]
Transitional Unit Messinian	Alcalá de Guadaíra (Seville)	Mysticeti	Cranium, vertebrae, ribs, scapulae, tympanic bullae, jaws	Sendra et al. 1996 [50]
Lower Pliocene	Lepe (Huelva)	Mysticeti (Cethoteridae)	Fragments of neurocranium, jaws, tympanic bulla	Sendra et al. 1999, 2000 [52,53]
Lower Pliocene Huelva Sands	Bonares (Huelva)	Mysticeti	Fragments of neurocranium, jaws, vertebrae	Esperante et al. 2009 [20]

With the aim of improving knowledge of the late Neogene record of cetaceans and understanding the preservation processes that led to their fossilization, here we present a new exceptional finding discovered in the Lower Pliocene strata of the province of Cádiz.

2. Geological and Stratigraphic Setting

The study area is located along the Atlantic coast of Andalusia (SW Spain) between the Guadalquivir River mouth and the town of Conil de la Frontera (Figure 1). Geographically, it belongs to the Gulf of Cádiz, whereas it is part of the Guadalquivir Foreland Basin geologically. The sedimentary units exposed at the study site include (1) a stratigraphically lower stratal package consisting of preorogenic materials from the Betic Mountain Range

(Permian–Lower Miocene) and synorogenic deposits from the Guadalquivir Olistostrome Complex (Lower–Middle Miocene) and (2) a stratigraphically higher succession of postorogenic materials (Upper Miocene–Quaternary) that were deposited after the Alpine Orogeny in the marine environments of the Guadalquivir Basin [57,58].
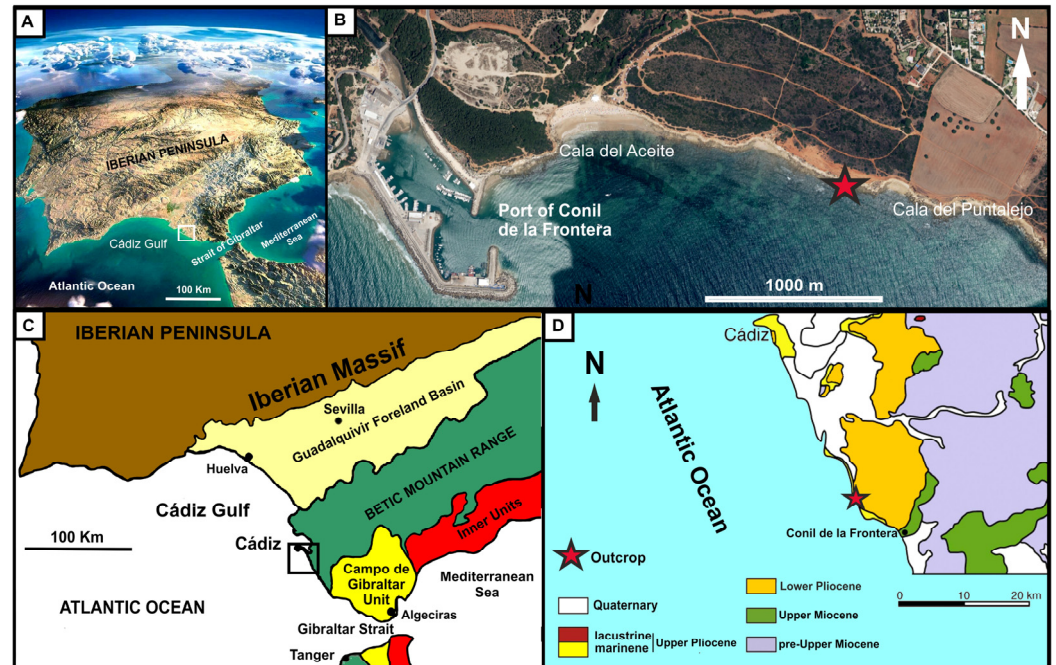
Figure 1. Geographical and geological setting of the study area. (**A**) Satellite image of the Iberian Peninsula. (**B**) Satellite image of the Cádiz Gulf. The red star indicates the position of the fossil remains. (**C**) Geological scheme of the southwestern part of the Iberian Peninsula. (**D**) Geological map of the study area.

During the early Messinian, a compressional regime caused the uplift of the Betic and Riff mountain ranges, resulting in a marine regression as well as an interruption of the communications between the Atlantic Ocean and the Mediterranean Sea (one of the causes of the Messinian Salinity Crisis) [59–62]. A later extensional phase caused the subsidence of part of the Gibraltar Arch and the re-establishment of communications between the Atlantic and Mediterranean [63]. Following a rapid sea-level rise, sedimentation began again. During the Early Pliocene, the Guadalquivir Basin was occupied by a gulf that opened southwards, i.e., onto the Atlantic Ocean, where sandstones were deposited in shallow-marine environments. Later, between the Late Pliocene and the Pleistocene, gravel and sands were deposited in coastal environments [64,65]. In the western sector of the Guadalquivir Basin, north of the study area, the post-Messinian sedimentary fill comprises fluvial and aeolian deposits.

The studied outcrop belongs to the post-Messinian deposits and is located along the cliffs stretching northwest of Conil de la Frontera (Cádiz, Spain), between Cala del Aceite and Cala del Puntalejo (Figure 1). From bottom to top, the exposed units are the following: Unit I, Unit II, and Unit III (see Figure 2).
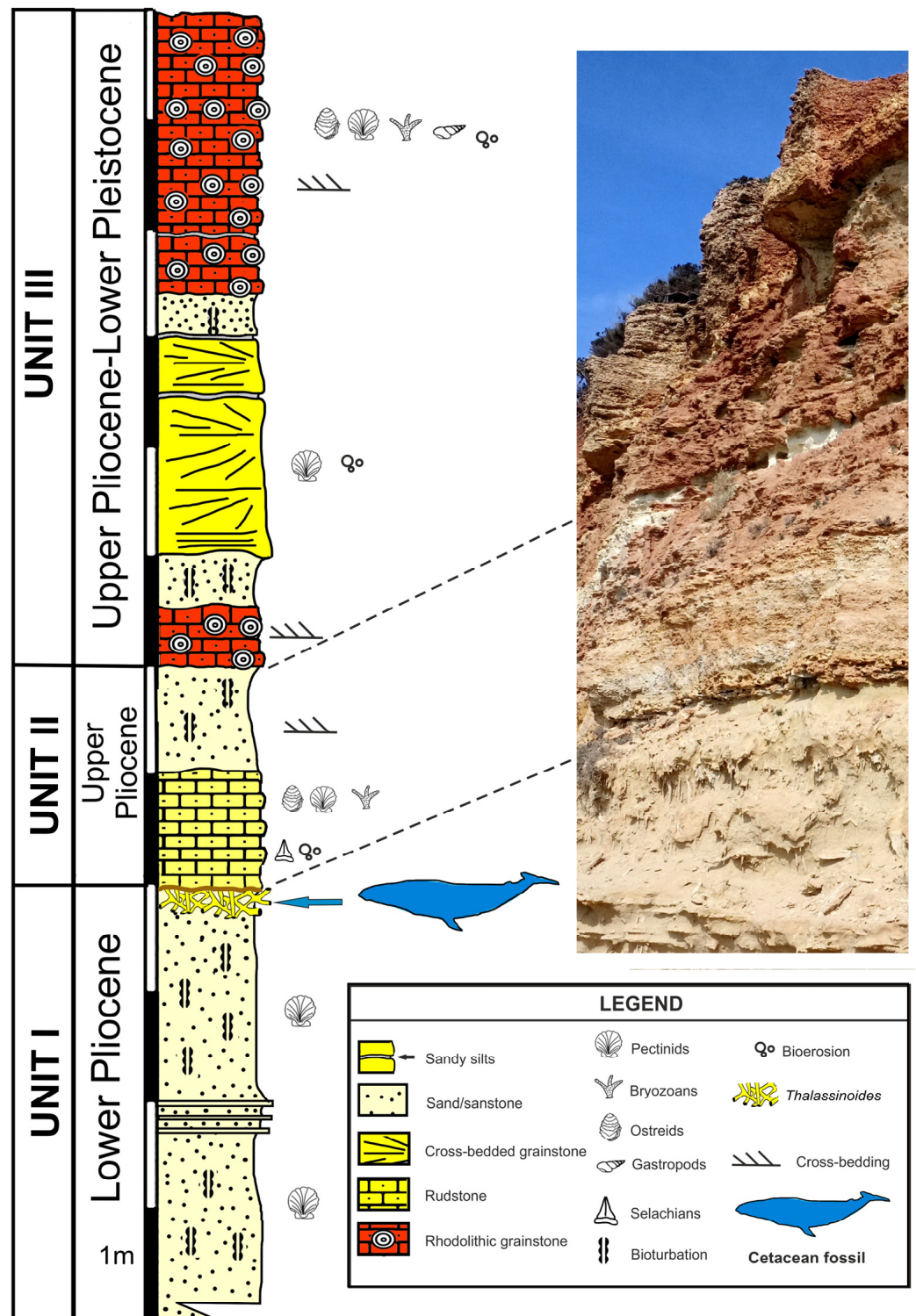
Figure 2. Measured stratigraphic column of the Pliocene–Pleistocene studied outcrop and outcrop field photo, with indication of the stratigraphic position of the cetacean remains.

Unit I begins with two meters of fine sand and grayish silt with interbeds of cemented layers with normal grading, about 10 cm in thickness. These basal sediments are intensely bioturbated (index 3–4 of [66]) and mainly characterized by the ichnotaxon *Cylindrichnus concentricus* (see [67] for more details). Unit I features a dispersed fauna formed specifically by pectinids such as *Amussium cristatum* and *Chlamys multistriata*, in addition to other fossils such as *Ostrea edulis* and balanid barnacles, which are disarticulated and with

the skeletal elements parallel to the stratification plane. The top of this unit is intensely bioturbated and features the abundant presence of the ichnotaxon *Thalassinoides* isp. The upper part of this bioturbated interval includes a hardground layer that runs continuously throughout the outcrop with a thickness of 1–2 cm. This unit has been attributed to the Lower Pliocene [65,68] and is the main subject of this study since it includes the analyzed whale fossil.

Unit II begins with a layer of calcirudites that fill *Thalassinoides* burrows in the underlying Unit I (Figure 2). This deposit passes upwards into a bioclastic rudstone with abundant fossils such as *Ostrea edulis*, *Pecten jacobaeus*, *Pecten benedictus*, *Chlamys multistriata*, *Glycimeris* sp., *Mytilus* sp., balanid barnacles, serpulids, and regular echinoid radioles, as well as few selachian teeth belonging to broad-toothed members of *Carcharhinus*. Fossils do not display a preferential orientation and are generally fragmented, bioeroded (mainly by pervasive *Entobia* isp.), and encrusted (mainly by balanids). The upper part of this unit consists of one meter of quartz-rich sand with large-scale cross-stratification. In the upper part of the sandy stratum, centimeter-thick silt layers are interspersed with channeled bodies with abundant bioclasts. The unit ends with a layer of barren cross-stratified fine sand. Unit II is attributed to the Upper Pliocene [65,68].

Unit III rests through an angular and erosive unconformity on Unit II. It is formed by an alternation of sands, grainstone, and rhodolithic grainstone with cross-stratification. The rhodoliths of this unit are formed by coralline algae, serpulids, bryozoans, and vermetids. Unit III has been attributed to the Upper Pliocene–Lower Pleistocene [65,67–69].

3. Data Gathering and Research Methods

3.1. Field Data Collection

The fossil whale dealt with in the present paper was found at the locality of Conil de la Frontera (Cádiz, Spain) between Cala del Puntalejo and Cala del Aceite (Figure 1). The taphonomic analysis was facilitated by the fossil skeleton being naturally exposed, although the description was hampered by extensive weathering of the bones in the present-day subaerial environment. For this reason, fossil bones were not excavated but only gently cleaned with brushes and paleo-tools.

Macroscopic taphonomic data were collected in accordance with Bianucci et al. [26] and Bosio et al. [18] using the taphonomic sheet reported in Figure 3. Taphonomic descriptors include the degrees of skeletal articulation and completeness, the orientation and disposition of the specimen, the presence of bioerosional features (e.g., bite marks on bone), the associated fauna, the extent of recent erosion, and the sedimentary features of the depositional environment. The collected data also include some measurements, such as the total length of the skeleton. The degree of fusion of the vertebral epiphyses was also evaluated (a proxy for physical maturity) [70,71]. Three bone samples were collected from the ribs for microtaphonomic analyses, namely, CA-OS1, CA-OS2, and CA-OS3. The field taphonomic data recorded for the fossil whale are shown in Figure 3.

A detailed sedimentary log was measured at the decimeter scale using a Jacob's staff. Sediment color, grain size, fossil content, and sedimentary structures were accurately described. The studied whale was then positioned along the measured stratigraphic section. Samples from the three different strata observed in the block where the fossil whale occurred were sampled in the field. These samples are named, from oldest to youngest, as CA-PE2, CA-PE1, and CA-PE3.
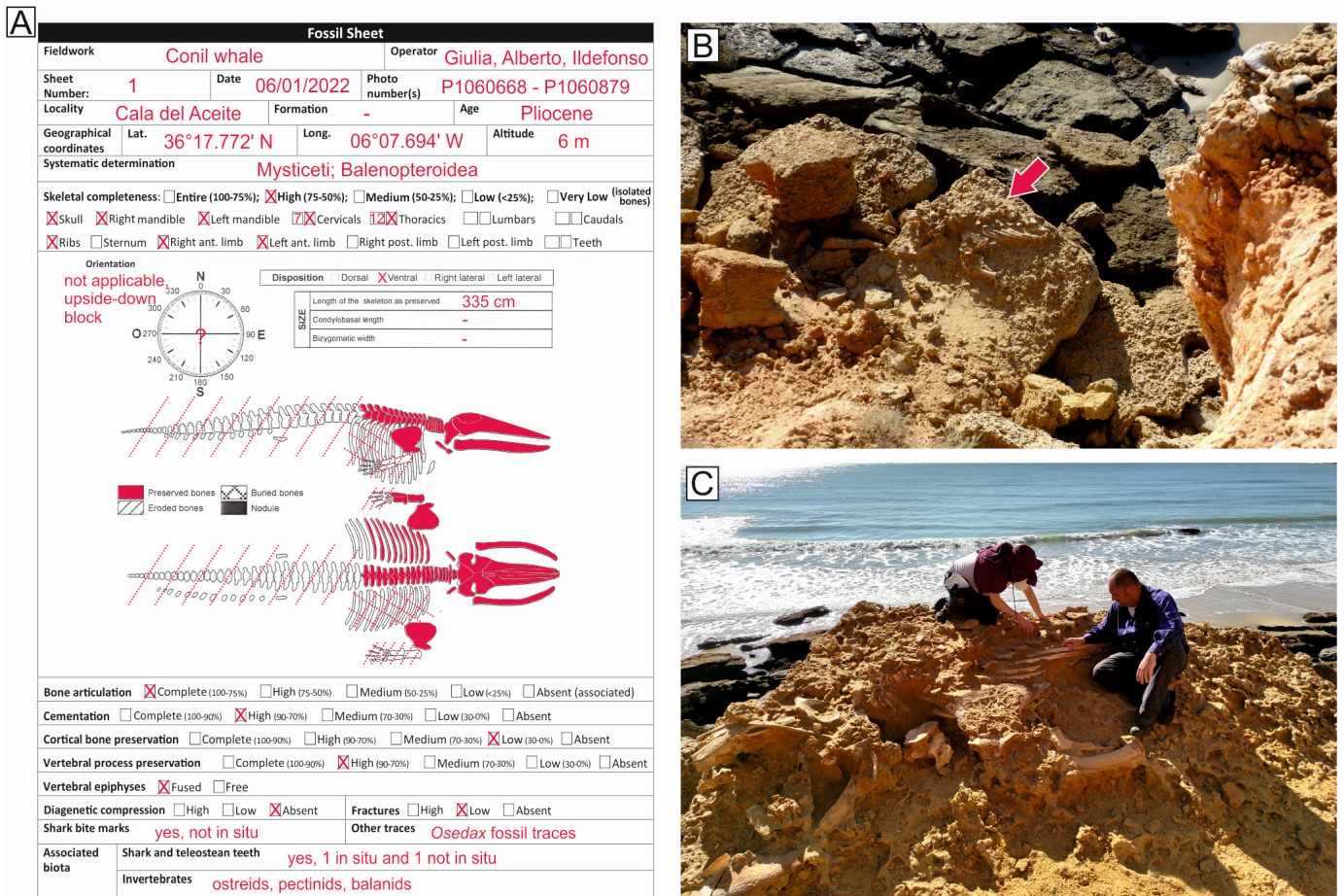
Figure 3. Taphonomic sheet and field photos of the Cádiz fossil whale. (**A**) Taphonomic sheet with field taphonomic observations. (**B**) Field photo of the block on which the skeleton occurs, taken from the top of the nearby cliff. (**C**) Field photo of the fossil remains of the studied mysticete skeleton, with researchers shown for scale.

3.2. Analytical Methods

Thin sections from bone fragments of the fossil mysticete and sediment samples from the three strata were prepared at the laboratories of TS Lab & Geoservices in Cascina, Pisa Province, after embedding them in epoxy resin. Two oyster samples were also prepared for the diagenetic evaluation preliminary to the sample selection for SIS (Strontium Isotope Stratigraphy) analyses. Thin sections were analyzed through a Nikon Eclipse LV100N POL transmitted light optical polarizing microscope at the Università degli Studi di Milano-Bicocca. Thin sections of sediment were analyzed in order to better define the sediment composition. The skeletal assemblages were assessed based on visual comparison charts for percentage estimation [72,73]. Bone and oyster thin sections were also analyzed via scanning electron microscopy (SEM) and energy-dispersive X-ray spectroscopy (EDS) using a Zeiss FEG Gemini 500 equipped with an EDS Bruker XFLASH 6/30 at the Università degli Studi di Milano-Bicocca. Backscattered electron (BSE) images and compositional analyses of major elements were realized in order to determine the chemical composition of the bones and cements. The SEM–EDS analytical conditions were 15 kV accelerating voltage, 5 pA beam current, and 8 mm working distance.

Oyster specimens were analyzed macroscopically and microscopically to evaluate their preservation state and screened for diagenetic alteration. Five oyster specimens were chosen for applying SIS. To better assess the contribution of diagenetic alteration, one "control sample" was also collected from the bulk sediment. Following Bosio et al. [74], oyster specimens were cleaned in distilled water in an ultrasonic bath to remove extraneous

particles. After drying, the shells were pulverized using a Dremel microdrill equipped with a 0.8 mm diamond tip. A few milligrams of powder were collected from each oyster, avoiding contamination, and sent to the laboratories of the Ruhr-Universität Bochum. Here, samples were firstly analyzed via ICP-OES (inductively coupled plasma optical emission spectroscopy) through a Thermo Fisher Scientific iCAP 6500 DUO spectrometer for measuring minor element concentrations. Then, samples were analyzed through a TI-Box (Spectromat) thermal ionization mass spectrometer (TIMS) with seven collectors for determining $^{87}Sr/^{86}Sr$ ratios using a dynamic (peak-hopping) mode of measurement. The cut-off limit for a strontium run was an error of $\pm 2\sigma \leq 5 \times 10^{-6}$ for the $^{87}Sr/^{86}Sr$ ratio, with 100–200 ratios per run (typical duration: 110 ratios, lasting 2 h and 15 min, plus the filament heating time). NIST NBS 987 and USGS EN-1 were employed in the analyses as standards, with a long-term mean measured at Bochum of 0.710246 ± 0.000027 (2σ) and 0.709163 ± 0.000037 (2σ), respectively. Rubidium abundances were monitored during the entire run; when Rb levels surpassed the detection limit, the result was discarded. $^{87}Sr/^{86}Sr$ data were corrected for the difference between the USGS EN-1 value used for the compilation of McArthur's reference curve and the USGS EN-1 Bochum mean value. $^{87}Sr/^{86}Sr$ corrected values were converted into ages using the LOESS Table 6 calibrated to the GTS2020 timescale [75]. To estimate the age of the stratigraphic layer, a mean $^{87}Sr/^{86}Sr$ value was calculated from the better-preserved oysters and then converted to age [76,77]. The uncertainty was calculated as 2 s.e. (standard errors) from the standard deviation of the mean value. For each estimation, a maximum age, a preferred age, and a minimum age were obtained.

A system of 3D photogrammetry through the use of a drone was used as the methodology for the 3D documentation of the whale. The system used has different variables that need to be controlled or at least be within acceptable ranges. In the first place, the aircraft used should be adapted to this type of work with some minimum requirements with regard to the quality of the image taken. In this case, we used equipment sold by the manufacturer DJI, i.e., the PHANTOM 4PRO, which is equipped with a 20 MP camera. Meteorological factors must also be taken into consideration given that the drone can operate within a temperature range of 0 to 40 °C and with wind gusts of up to 10 m/s. Before the acquisition, the planning of the flight took place on land, with authorization requested from the Ministry of Defense to photograph part of the MTN page E: 1/25.000, number 1073-1. Subsequently, and taking into account the relatively small surface, three flights were carried out at three different heights, i.e., 5, 10, and 15 m, with a total of 150 photographs being taken at different angles with respect to the fossil-bearing surface. These photographs overlapped for more than 40% and less than 75%. Thanks to this overlap, a photogrammetric collage could be made because the algorithm used by the software specializing in image treatment carries out a search for equivalent points in the image to carry out a reconstruction of the 3D scene. The most common algorithm to carry out this steep is the SIFT technique (scale-invariant feature transform; [78]). In this case, and due to the flight surface, it was not necessary to use support points. Each image has a center with known geographical coordinates, which are taken by the very same aircraft, and after finding the coinciding points, a tridimensional model can be built of the photographed surface, obtaining a cloud of georeferenced points [79]. All this work of composing three-dimensional images was carried out with the Agisoft Metashape (Photoscan) software (version 1.7.0.). The 3D reconstruction of the fossil whale can be accessed through the Supplementary Material.

4. Results

4.1. Taxonomy and Ontogenetic Status

Characters such as a highly telescopic cranium, the narrow and elongated ascending processes of the maxillae exposed at the cranium vertex, and an anteriorly extended occipital shield that likely overhung the rest of the neurocranium indicate that the studied skeleton belongs to the superfamily Balaenopteroidea of baleen-bearing whales (Mysticeti) and possibly to the rorqual family Balaenopteridae. The specimen exhibits the complete

fusion of all the vertebral epiphyses to the corresponding vertebral centra, which suggests an adult mysticete.

4.2. Articulation and Completeness

The largest portion of the skeleton has undergone breakage after the detachment of the block from the cliff as well as prolonged erosion in the present-day subaerial environment (Figures 3 and 4). The fossil specimen has a total length of 335 cm and includes 7 cervical vertebrae (Figure 5D) and ca. 12 thoracic vertebrae; ca. 10 left ribs (Figure 5G,H); both the scapulae (Figure 5E,F) (the right one is ex situ); the left humerus, radius and ulna (Figure 5E); and an essentially complete cranium, including the hyoid, maxilla, premaxilla, nasal, frontal, occipital, squamosal, parietal, presphenoid, vomer, lacrimal, jugal, and mandible (Figures 4 and 5A,B). The two tympanic bullae are also preserved. Considering the five classes for the degree of skeletal completeness proposed by Bosio et al. [18] (i.e., 4, 75–100% of the skeleton preserved; 3, 50–75% of the skeleton preserved; 2, 25–50% of the skeleton preserved; 1, <25% of the skeleton preserved; 0, isolated bone or compound skeletal element as the cranium), the examined specimen belongs to the completeness class 3. This value is most likely related also to the recent erosion and breakage of the skeleton. In fact, part of the thoracic vertebrae and all the lumbar and caudal vertebrae were completely lost due to the breakage of the block. In addition, the right ribs might be buried within the sediment and, as such, completely hidden to surface prospecting. However, some lost elements might be related to the gradual detachment of the skeletal parts fallen to the seafloor, e.g., the forelimb bones; all the phalanges; and probably the right humerus, radius, and ulna.
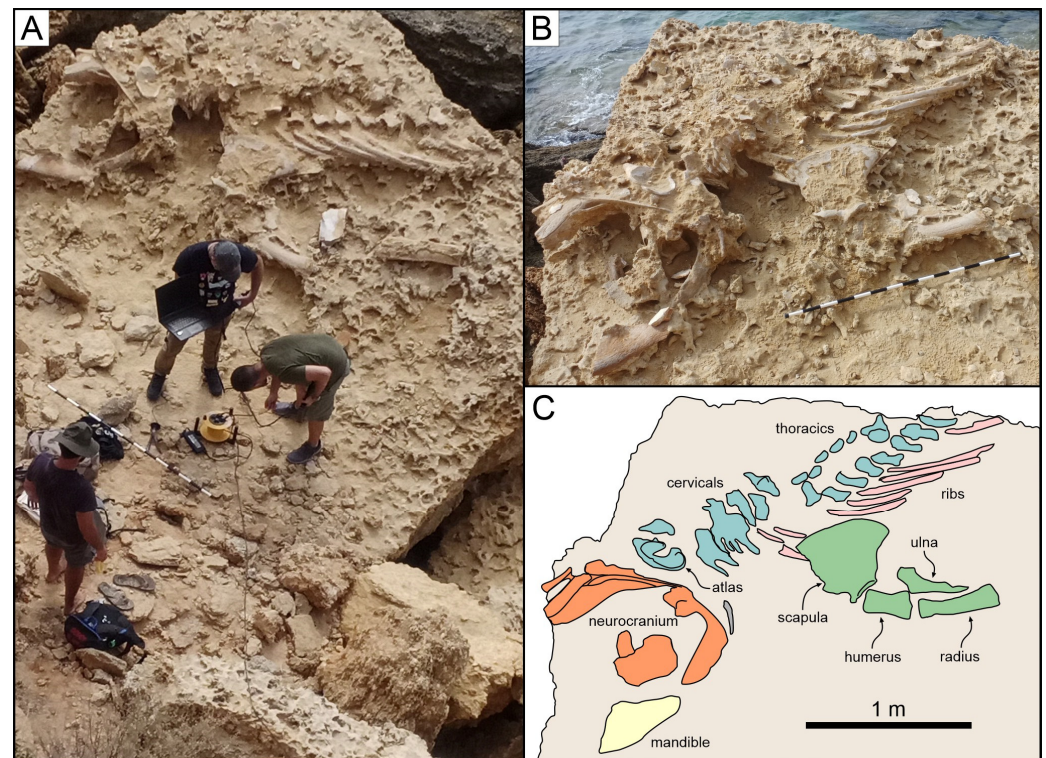
Figure 4. Field photos and explanatory line drawing for the studied fossil whale. (**A**) Field photo of the drone survey for the 3D reconstruction of the mysticete skeleton. (**B**) The main portion of the fossil skeleton of the mysticete. (**C**) Explanatory line drawing of the anatomical parts from a direct interpretation of the mysticete skeleton shown in panel B.
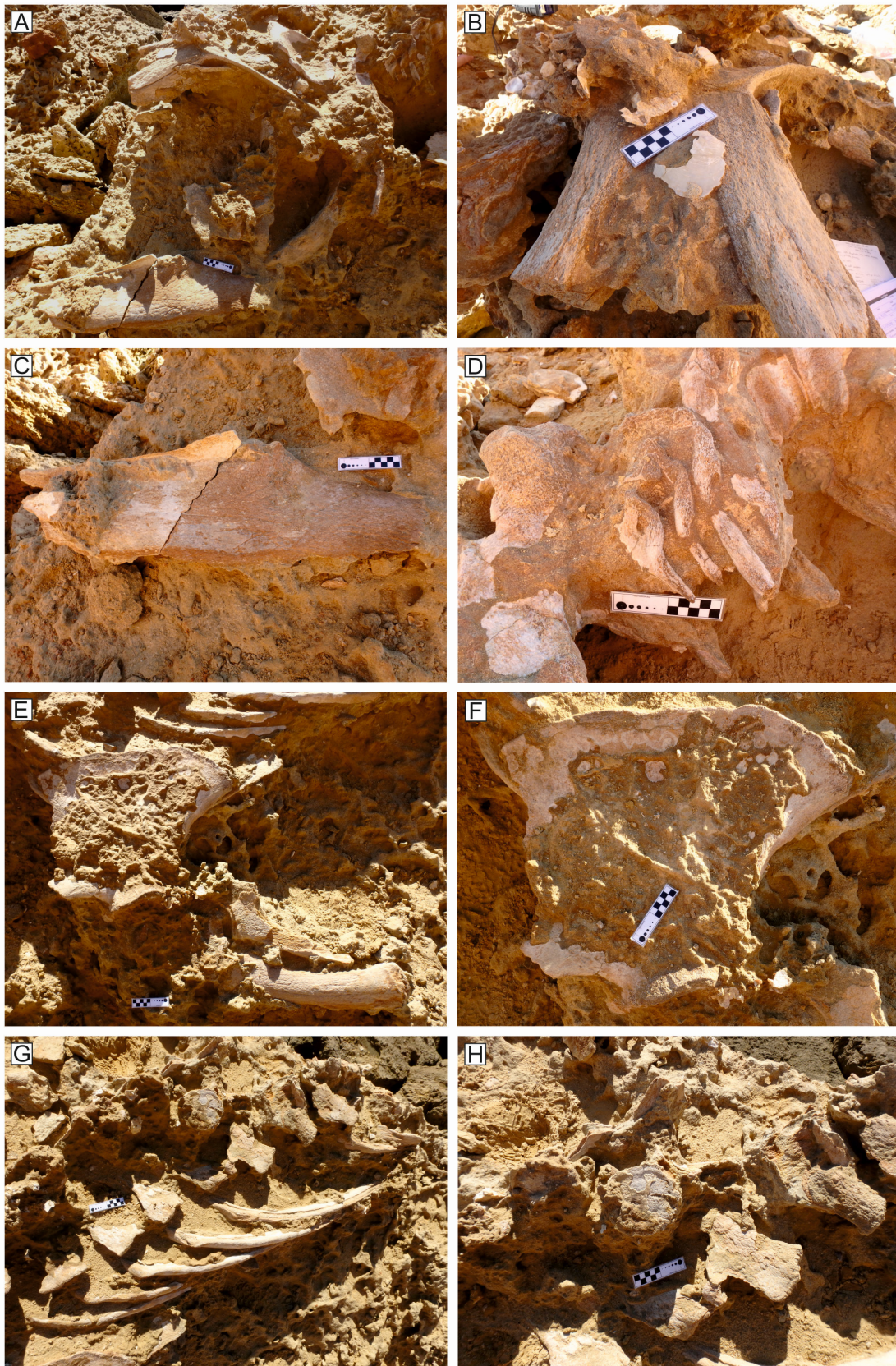
Figure 5. Detailed field photos of the studied fossil remains. (**A**) Neurocranium and left mandible. (**B**) Close-up of the skull vertex. (**C**) Close-up of the left mandible. (**D**) Close-up of the cervical vertebrae. (**E**) Close-up of the left limb. (**F**) Close-up of the left scapula. (**G**) Thoracic vertebrae and ribs. (**H**) Close-up of the thoracic vertebrae, exhibiting a disarticulated vertebra.

Considering the articulation degree, the skeleton displays a complete articulation with regard to the cranium and mandibles, most of the vertebrae, the ribs, and the forelimbs, whereas the atlas and one thoracic vertebra are dislocated, lying dorsal side up. Therefore, following the five classes describing the degree of skeletal articulation proposed by Bosio et al. [18] (i.e., 4, 75–100% of the bones articulated; 3, 50–75% of the bones articulated; 2, 25–50% of the bones articulated; 1, <25% of the bones articulated; 0, bones fully disarticulated), the specimen can be attributed to the articulation class 4.

4.3. Disposition

The detachment of the block from the cliff makes any estimation of the original orientation difficult. The skeleton is NW–SE oriented, which is substantially parallel to the present-day coast. Paleo-storm currents are indeed reconstructed to hail from southeast and southwest [67].

Although the skeleton is currently observed laying dorsal side up, the original general disposition of the skeleton was belly-up (ventral side up) on the seafloor, which suggests a reflotation of the carcass after death [8]. However, a slight degree of displacement is observed. Behind the cervicals, the rest of the vertebral column is slightly laterally tilted, with the neural processes projecting horizontally and parallel to each other (Figures 3, 4 and 5G,H).

4.4. Shark Tooth Marks and Associated Shark Teeth

The bones of the Cádiz whale do not usually preserve the cortical bone tissue (see Section 4.6) except in a few areas, thus allowing the observation of some trace fossils. In one of these cases, two shark tooth marks (sensu Zonneveld et al. [80]) are observed on one rib fragment that was not found in situ. The two marks are roughly parallel to the long axis of the bone and are referable to the morphological genetic types I or II (sensu [81–83]). These traces are deep, elongated, relatively straight to broadly arched, and up to 3 cm long (Figure 6A). The size and depth of the tooth marks are suggestive of a large macrophagous shark.

Interestingly, two shark teeth were found near the whale skeleton. The first one was found in situ, near the zygomatic process of squamosal, and is here identified as belonging to *Carcharhinus* cf. *leucas* (Figure 6B,C); the second was found ex situ, fragmentary, and recognized as belonging to a member of Carcharhiniformes.

4.5. Associated Macroinvertebrates and Macroinvertebrate Traces

Where the cortical bone tissue is preserved, some fossil invertebrate traces are observed. Two overlapping rib fragments that were found ex situ display clustering, rounded pits. These are roughly circular to somewhat elliptical pockmarks with a diameter ranging from less than 1 mm to 1 cm (Figure 6D,E). These traces are interpreted herein as collapsed boreholes of the siboglinid annelid *Osedax* sp., which is also known as the "zombie worm" [84,85]. These traces are usually punctiform on the bone surface and expand into the bones to form three-dimensional chambers with a typical broccoli-like morphology, which goes under the ichnogeneric name *Osspecus* [86]. In some cases, as observed for the Cádiz whale, the numerous boreholes can merge with each other and consequently lead to the collapse of the surface layer of the cortical bone, resulting in a pitted texture of the bone surface [87,88].

The skeleton is partly covered by the complete shells of different macroinvertebrates, whereas in the surrounding sediment (i.e., both the *Thalassinoides* layer and the lower sandstone layer), invertebrates are represented by shell fragments. This faunal assemblage mainly consists of balanid barnacles, bivalves such as ostreids and pectinids, and brachyuran decapod crustaceans (Figure 6F,G). It is noteworthy that the encrusting barnacles display considerable size range, from a few millimeters up to four centimeters in diameter, thus indicating that the skeleton was exposed for quite a long time before burial.

Likewise, a decapod chela (i.e., crab claw) was also found near the skeleton, possibly a remain of the inhabitants of the *Thalassinoides* burrows (Figure 6H).
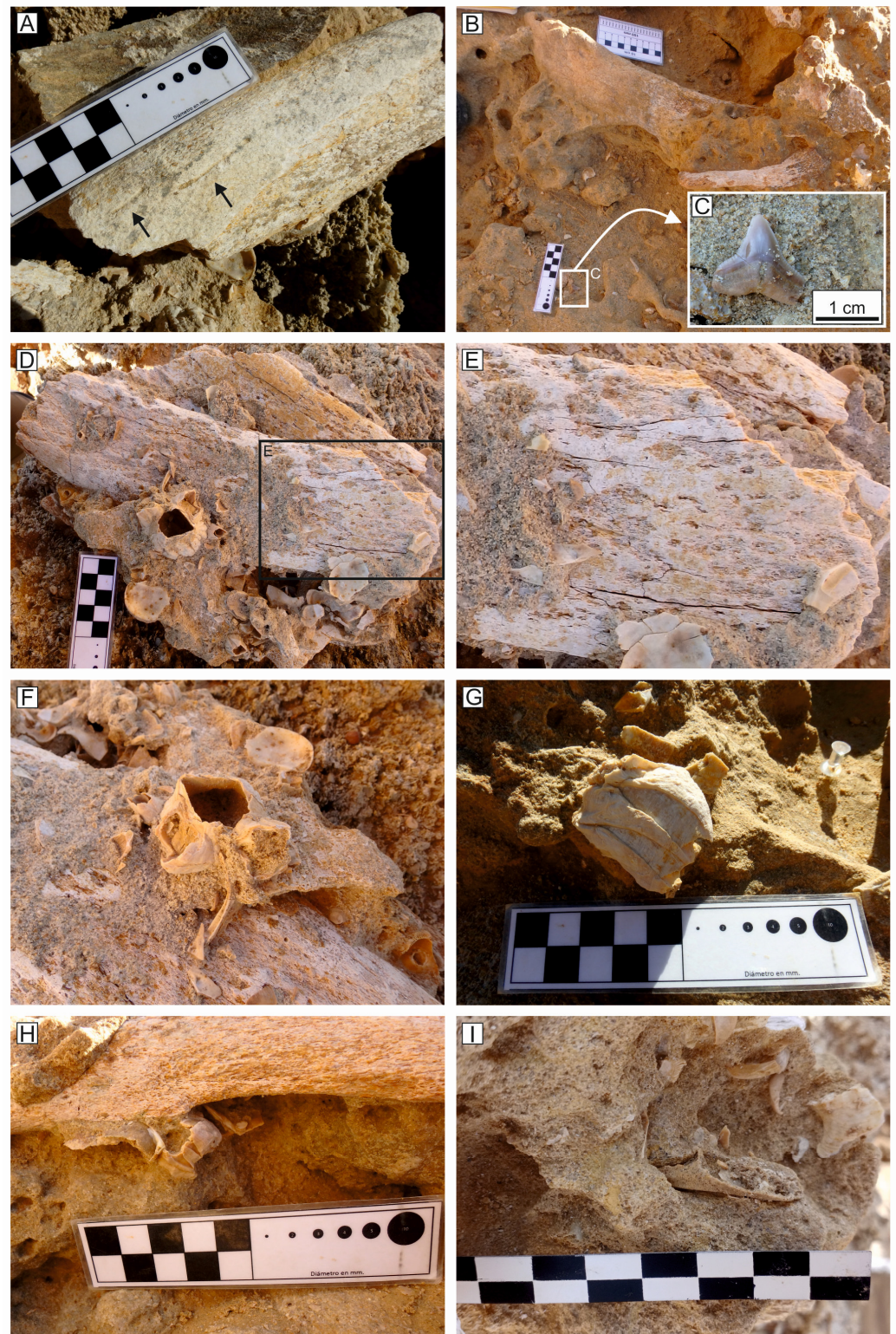

Figure 6. Taphonomic features of the fossil whale. (**A**) Close-up of the two shark tooth marks on a rib. (**B**) Tooth of *Carcharhinus* cf. *leucas* found near the zygomatic process of squamosal. (**C**) Close-up of the tooth depicted in Figure 6B. (**D**) Clustering round pits that can be referred to collapsed holes of *Osedax* sp. (**E**) Close-up of the boreholes depicted in Figure 6D. (**F–H**) Balanid barnacles encrusting bones. (**I**) A decapod claw found in the vicinity of the skeleton.

4.6. Bone Preservation and Mineralization

Bones are moderately preserved, with a high vertebral process preservation (ca. 70–90%, see Figure 3) and no evidence of diagenetic compression. Fractures are common but mostly attributable to erosion and breakage during the recent subaerial exposure. The degree of cortical bone preservation is low (<30%, see Figure 3) and not only where the recent erosion took place (Figures 5 and 6). Bones exhibited a pinkish color that persists under the microscope, where the bone is was light brown with local reddish areas (Figure 7A). The reddish color is related to the presence of abundant iron oxide or pyrite particles (see below).

At the microscale (both optical microscope and SEM), bones preserve the original microstructure with compact bone and cancellous bone tissues and their histological features, such as primary and secondary osteons, osteocyte lacunae, and lamellae (Figure 7A–E). Bones show a moderately mineralized bone tissue based on the average atomic weight revealed by the grayscale of the BSE imaging [10,89]: some areas are locally fragile with a low to moderate mineralization degree (Figure 7B); others exhibit a highly mineralized tissue with brighter areas, suggesting the presence of Fe oxide grains in the bone tissue (Figure 7C). In particular, some osteocyte lacunae are occupied by Fe oxides, which also fill the very thin canaliculi (Figure 7D,E). EDS analyses indicate that the bone tissue composition is Ca phosphate, with an increase of Fe content in the brighter zones (Table 2). In some cases, Fe oxides seem to also replace bone tissue concentrically at the edge of the osteons, especially when the Haversian canal is filled by iron minerals (Figure 7F). This type of replacement was reported by Pfretzschner [90,91] to happen during late diagenesis, hence in a different time with respect to the early pyrite precipitation of framboids. Iron minerals are also detected in the form of framboids lining or partially filling the Haversian canals and intertrabecular medullary cavities, also being interspersed in the sediment adjacent to the bone (Figure 8A–D). These opaque minerals, displaying a high brightness in BSE imaging, are revealed to have a Fe oxide composition through EDS analyses (Table 2). However, some framboidal Fe oxides probably represent relics of original pyrite framboids.

Bone cavities, i.e., the Haversian canals of the compact bone and the intertrabecular medullary cavities of the cancellous bone, exhibit a partial or complete filling by a carbonate cement showing a mosaic texture (Figure 8E,F), which is typical of secondary minerals precipitated during late diagenesis [10]. The EDS analyses confirm that the cement consists of calcite (Table 2). In addition, intertrabecular medullary cavities are usually occupied by sediment particles (mainly quartz grains), benthic and planktic foraminifera, and rare echinoid radioles (Figure 9A). The interstitial fraction is formed by calcite cement close to the bone tissue, whereas the matrix occurs further from the bone. Sediment particles could have entered the bone cavities with seawater, likely due to being sucked in by the escaping of gas bubbles (which in turn originates from the decomposition of organic matter [92]) or by entering broken bone tissues exposed on the seafloor before burial. The latter seems the case for some of the analyzed bones as the trabeculae display pervasive cracks (Figure 9A). Microfractures are common but usually distributed regardless of the histological microstructure and, as such, not related to early diagenesis (i.e., the radial microcracks of Pfretzschner [93]).
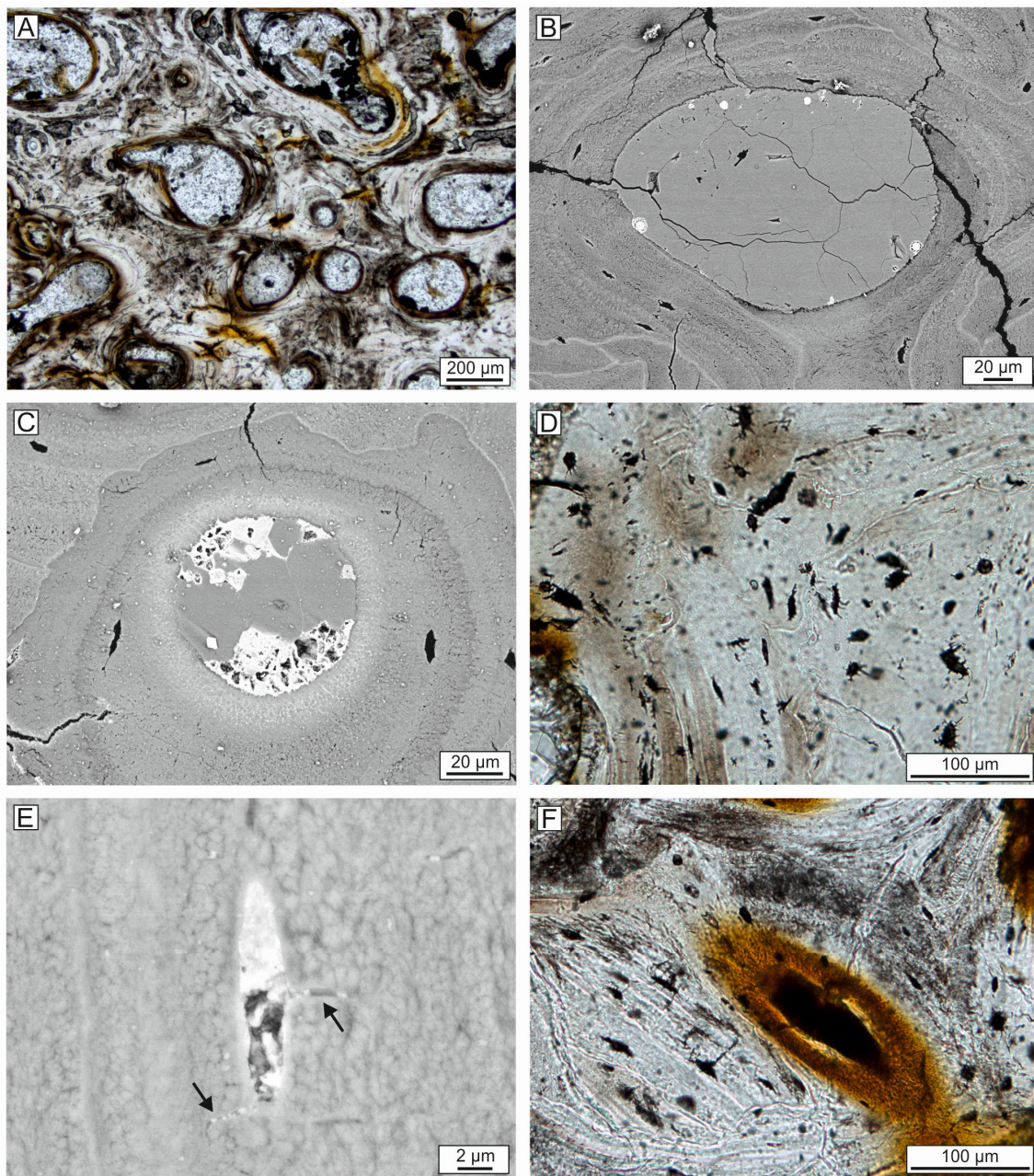
Figure 7. Bone photomicrographs and SEM images showing histological features. (**A**) Compact bone under transmitted plane-polarized light. Note the histological features and the pink/light brown color of the bones with reddened portions. (**B**) BSE image of an osteon showing a low to moderate mineralization, a cement filling the Haversian canal, and Fe oxide framboids. (**C**) BSE image of an osteon showing a moderate to high mineralization and a cement filling the Haversian canal with Fe oxides. Note the brightness of the bone surrounding the Haversian canal enriched in Fe. (**D**) Close-up of osteocyte lacunae under transmitted plane-polarized light. Note the Fe oxide filling of the lacunae and canaliculi. (**E**) Close-up of an osteocyte lacuna partially filled by Fe oxides. Black arrows indicate the Fe oxide filling of the canaliculi. (**F**) Close-up of an osteon under transmitted plane-polarized light. Note the Fe oxide filling of the Haversian canal and the reddish color of the bone in the vicinity.
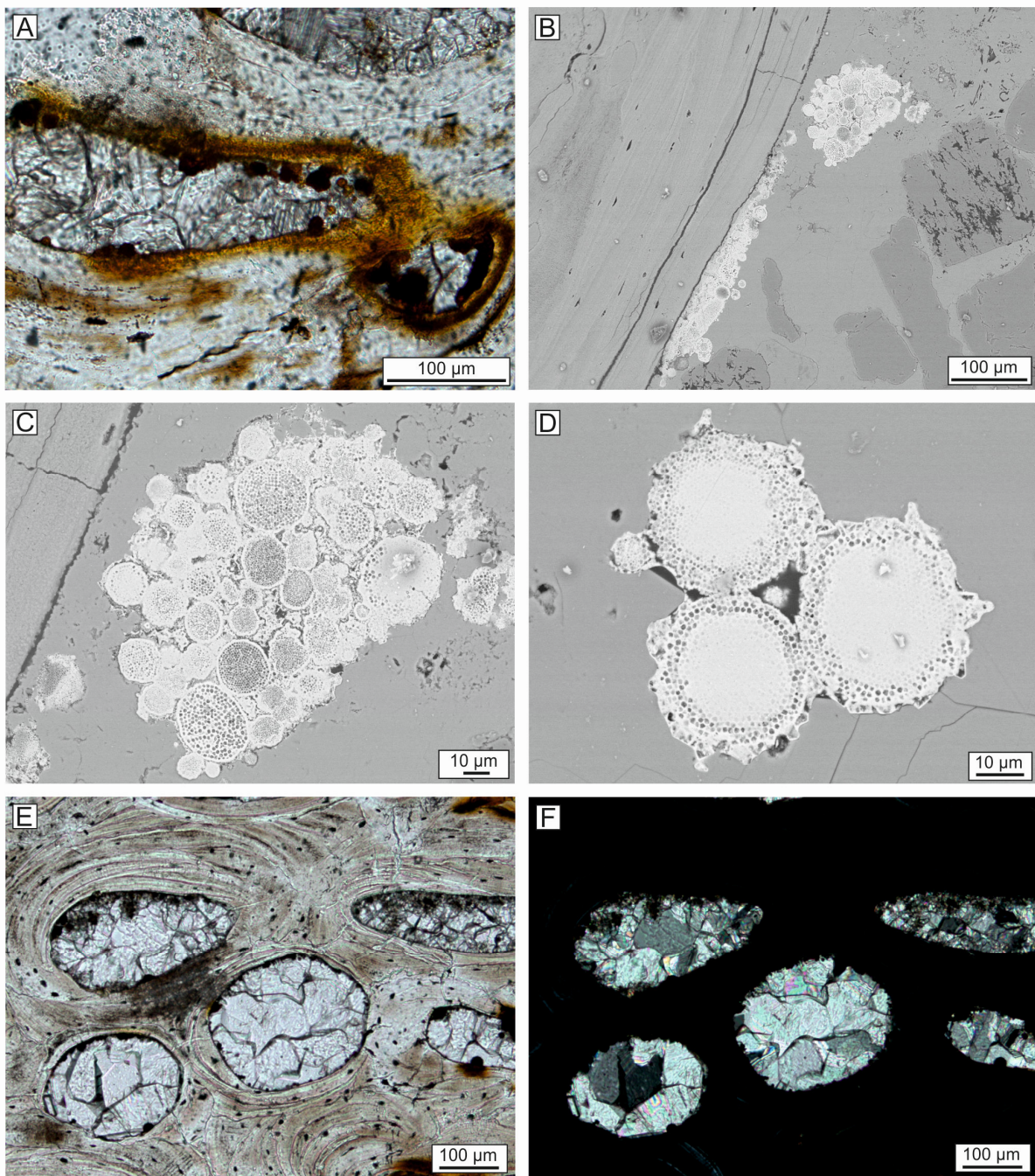
Figure 8. Bone photomicrographs and SEM images showing diagenetic minerals. (**A**) Compact bone under transmitted plane-polarized light. Note the Fe oxide and calcite filling of the Haversian canal as well as the reddish color of the surrounding bone tissue. (**B**) Fe oxide framboids aligned along the boundary between the bone tissue and the sediment. (**C**) Close-up of Figure 8B showing Fe oxide framboids. (**D**) Close-up of the Fe oxide framboids in a calcite cement. (**E**) Compact bone under transmitted plane-polarized light, exhibiting Haversian canals filled by sparry calcite. (**F**) Same as Figure 8E under transmitted cross-polarized light, exhibiting Haversian canals filled by sparry calcite.
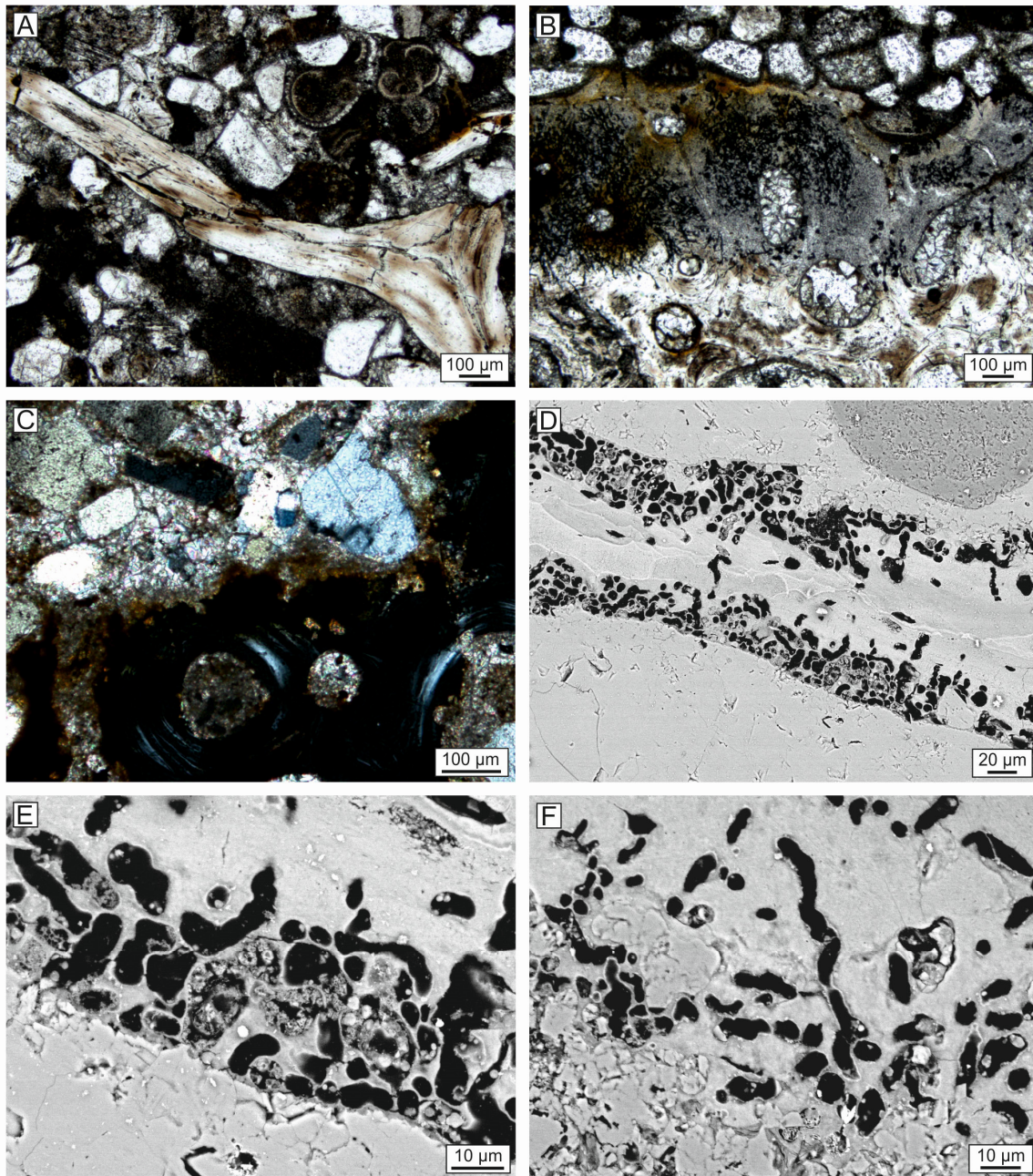
Figure 9. Bone photomicrographs and SEM images showing fractures, dissolution, and bioerosional features. (**A**) Bone trabecula under transmitted plane-polarized light, showing several fractures. Note the sediment that fills the intertrabecular cavities. (**B**) Compact bone under transmitted plane-polarized light, exhibiting dissolution traces affecting the external portion of the compact bone in contact with the sediment particles. (**C**) Close-up of the external portion of the compact bone under transmitted cross-polarized light. Note the dissolution traces on the bone part in contact with the sediment. (**D**) BSE image of type B microborings (sensu Gariboldi et al. [94] and Bosio et al. [18]). (**E**) Close-up of Figure 9B showing type B microborings. Note the brighter rim and the apatite infill. (**F**) Close-up of type B microborings. Note the brighter rim and the apatite infill.

Table 2. Chemical composition of the major elements (wt%) by means of energy-dispersive X-ray spectroscopy (EDS) of bone tissue, diagenetic cements, and iron minerals found in the bone cavities.

Sample	Type	P_2O_5	CaO	MgO	FeO	Na_2O	SiO_2	Al_2O_3	SO_3	Cl	Sum	Mineral
CA-OS1-1	cement	-	68.17	0.53	-	-	-	-	-	-	68.70	calcite
CA-OS1-2	bone	24.82	42.84	-	-	0.99	-	-	-	0.62	69.27	apatite
CA-OS1-3	bone	23.84	45.13	-	-	1.26	-	-	-	0.79	71.03	apatite
CA-OS1-4	bone	25.45	47.49	-	-	1.23	-	-	-	-	74.16	apatite
CA-OS1-5	cement	-	70.05	1.01	-	-	-	-	-	-	71.06	calcite
CA-OS1-6	framboid	-	1.33	-	70.24	-	4.35	0.98	-	-	76.90	Fe oxides
CA-OS1-7	bright bone	19.05	39.96	-	18.66	-	-	-	-	-	77.68	apatite
CA-OS1-8	bone	21.25	46.81	0.73	-	0.90	-	-	-	0.59	70.28	apatite
CA-OS2-1	bone	25.79	44.07	0.76	-	1.31	-	-	1.51	0.21	73.66	apatite
CA-OS2-2	bone	23.15	48.71	0.71	1.94	1.07	-	-	0.46	-	76.04	apatite
CA-OS2-3	cement	-	48.66	0.58	3.05	-	11.09	4.53	-	-	68.73	calcite
CA-OS2-4	bone	25.68	52.19	-	-	1.10	-	-	0.85	-	79.82	apatite
CA-OS2-5	microboring infill	21.67	50.47	-	2.85	0.94	-	-	-	-	75.94	apatite
CA-OS2-6	microboring infill	14.9	40.72	-	6.31	-	-	-	-	-	61.94	apatite
CA-OS2-7	microboring infill	24.44	38.82	-	5.40	-	0.46	0.73	0.56	0.86	73.44	apatite
CA-OS2-8	microboring infill	1.24	2.07	0.91	59.22	-	2.24	1.49	-	1.32	68.48	Fe oxides
CA-OS2-9	microboring infill	21.66	38.31	0.68	3.54	1.09	-	-	0.89	0.88	67.06	apatite
CA-OS2-10	microboring infill	14.83	40.83	0.73	6.85	1.07	-	0.58	0.55	0.67	66.12	apatite
CA-OS2-11	cement	-	76.33	-	-	-	-	-	-	-	76.33	calcite
CA-OS2-12	bone	22.60	51.68	0.78	-	2.67	-	-	-	-	77.72	apatite
CA-OS2-13	bone	27.68	48.73	-	-	0.91	-	-	0.69	0.22	78.23	apatite
CA-OS2-14	bright bone	17.78	53.54	0.56	8.06	0.76	-	-	0.53	-	81.21	apatite
CA-OS2-15	framboid	-	1.59	-	65.96	-	4.86	1.64	-	-	75.70	Fe oxides
CA-OS2-16	cement	-	74.38	-	-	-	-	-	-	-	74.38	calcite
CA-OS3-1	cement	-	75.38	-	-	-	-	-	-	-	75.38	calcite
CA-OS3-2	cement	-	73.02	-	-	-	-	-	-	-	73.02	calcite

The external portion of the compact bone is very poorly preserved, confirming the observations made at the macroscopic scale. In fact, under the microscope, the outer part of the compact bone that is in contact with the surrounding sediment is darker or reddish in color as well as irregular and pitted, indicating that it experienced dissolution and bioerosion (Figure 9B,C). Moreover, in some areas, numerous microborings are observed, both in the compact and cancellous bone tissue. Most microborings display a diameter between 3 and 9 μm and a length of ca. 20 μm. They are usually empty or filled by apatite or pyrite framboids and exhibit a slightly brighter rim in BSE images (Figure 9D–F). The EDS analyses indicate that the microboring infill composition is Ca phosphate with a higher Fe content with respect to the bone (Table 2). Given these characteristics, the studied microborings can be attributed to the type B sensu Gariboldi et al. [94] and Bosio et al. [18], which are interpreted as being related to bacterial sulfate-reduction activity [95]. The bone characteristics come closest to the bone type 2 as defined by Bosio et al. [10], with the exception of the bone color, which is not red but pinkish at the macroscale. However, under the microscope, red areas are present due to the occurrence of Fe oxides.

4.7. Composition of the Whale-Embedding Block

The block on which the whale skeleton rests comprises three different strata. These strata reflect, in an upside-down order, the succession exposed beneath the block itself (Figure 10A). The stratigraphically lowest stratum is a well-sorted, fine- to medium-grained sandstone (sample CA-PE2) with rare fossils (Figure 10B). The middle stratum is the *Thalassinoides*-bearing layer, which consists of a coarse- to very-coarse-grained calcarenite to calcirudite with an abundant fossil content (sample CA-PE1) consisting mostly of barnacles and mollusks (Figure 10C,D). The stratigraphically highest stratum is a calcirudite with an abundant fossil content (sample CA-PE3) consisting mostly of ostreids, pectinids, barnacles, serpulids, and bryozoans, in addition to rounded crystalline clasts and isolated cetacean bones (Figure 10E,F). The fossil whale is located in between the *Thalassinoides*-bearing layer and the well-sorted, medium-grained sandstone.
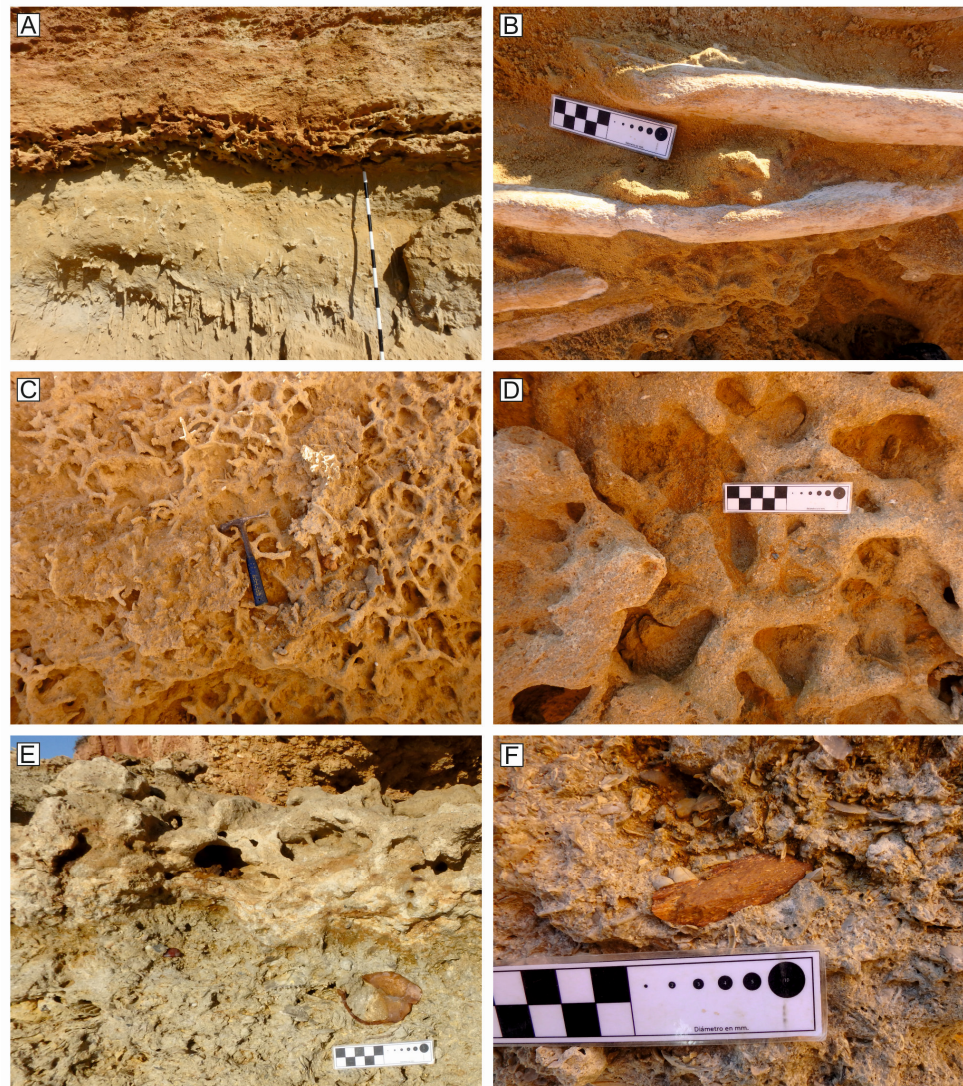
Figure 10. Field photos of the sediment associated to the studied fossil whale. (**A**) Outcrop view of the succession from which the whale-bearing block detached. (**B**) Field photo of the fine- to medium-grained sandstone hosting the studied cetacean skeleton (sample CA-PE2 was collected from this stratum). (**C**) Field photo of the calcarenite to calcirudite *Thalassinoides*-bearing layer (sample CA-PE1 was collected from this stratum). (**D**) Close-up of the *Thalassinoides*-bearing layer (sample CA-PE1 was collected from this stratum). (**E**) The three aforementioned layers occurring in an inverted order in another block that detached from the main outcrop. Note the occurrence of a cetacean bone (a tympanic bulla) in the stratigraphic higher calcirudite stratum (sample CA-PE3 was collected from this stratum). (**F**) Close-up of a fragmentary vertebrate bone in the calcirudite stratum (sample CA-PE3 was collected from this stratum).

At the microscale, sample CA-PE2 is characterized by very-fine- to medium-grained sand particles. It is clast-supported and comprises well-sorted, angular to subrounded terrigenous clasts, mainly consisting of quartz and rare feldspars. The fossil content is low and consists mainly of planktic foraminifera (including *Orbulina universa*) associated with rare benthic foraminifera (including *Lenticulina*). The interstitial fraction mainly consists of micrite associated with small patches of microsparite (Figure 11A). Sample CA-PE1 consists of clast-supported, moderately sorted, subangular to rounded, very-fine- to medium-sized, terrigenous sand clasts (mainly quartz). The bioclastic fraction is more significant than in CA-PE2 and consists mainly of mollusks, barnacles, and bryozoans associated with minor amounts of echinoids as well as planktic and benthic foraminifera. The interstitial

fraction mainly comprises sparite (Figure 11B). Sample CA-PE3 is characterized by clast- to matrix-supported, mixed siliciclastic–carbonate sediments with poorly sorted, subrounded to well-rounded, terrigenous clasts, mainly consisting of quartz, with a very-fine- to coarse-grained sand size. The bioclastic content is significant and consists mainly of mollusks, barnacles, and echinoderms associated with rare benthic foraminifera. The interstitial fraction is mainly micrite (Figure 11C).

The fossil whale is located in between the *Thalassinoides*-bearing layer (sample CA-PE1) and the underlying well-sorted, medium-grained sandstone (sample CA-PE2). In fact, the bone cavities are usually occupied by sediment particles mainly consisting of well-sorted quartz grains and fossils such as benthic and planktic foraminifera and rare echinoid spines (Figure 11D–F). The sediment surrounding the whale exhibited a high cementation degree (ca. 70–90%, see Figure 3).
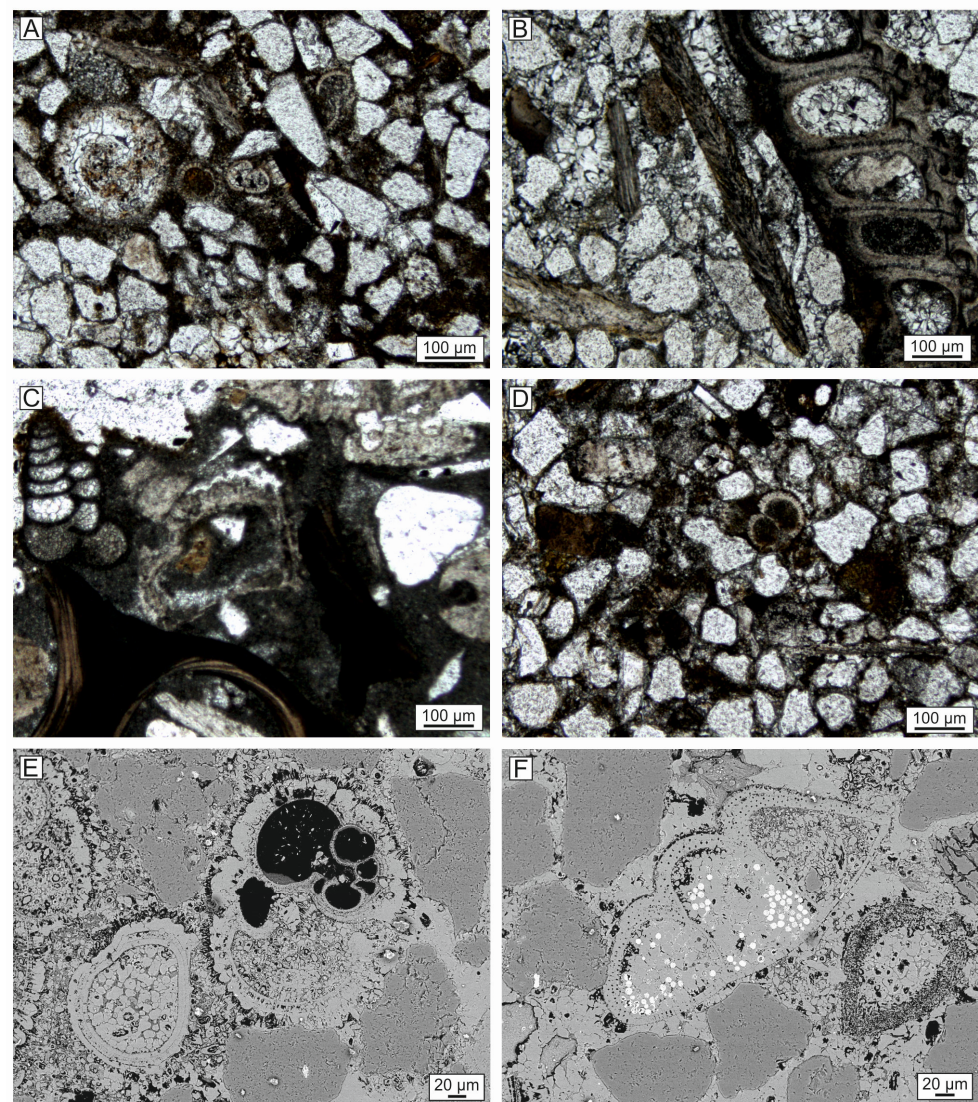
Figure 11. Photomicrographs of the sediment. (**A**) The CA-PE2 sandstone under transmitted cross-polarized light exhibiting terrigenous particles and planktic foraminifera. (**B**) The CA-PE1 calcarenite to calcirudite *Thalassinoides*-bearing layer under transmitted cross-polarized light. Note the barnacle and mollusk fragments. (**C**) The CA-PE3 calcirudite under transmitted cross-polarized light. Note the barnacle, mollusk and echinoid fragments, and a foraminifer. (**D**) The sediment surrounding bones under transmitted cross-polarized light exhibiting terrigenous particles and planktic foraminifera. (**E**) BSE image of planktic foraminifera cemented by calcite cement. (**F**) BSE image of a planktic foraminifer showing Fe oxide framboids and calcite cement in the internal chambers.

4.8. Strontium Isotope Stratigraphy

Fossil oysters from the same layer as the Cádiz whale are macroscopically well preserved, displaying unaltered nacreous layers and nor with macroscopic evidence of recrystallization, nor bioerosional features such as borings. Microscopically, the best-preserved samples, i.e., CA-OST2, CA-OST4, and CA-OST5, are characterized by calcite prismatic shell layers, whereas CA-OST1 exhibits an alternation of prismatic and vesicular shell structures (Figure 12A,B). The latter is diagnostic of the subfamily Pycnodonteinae and can be completely filled by secondary crystalline calcite [96]. For this reason, the sample CA-OST1 was excluded from the final age calculations. SEM–EDS maps confirm the calcite composition of the shells and highlight their attachment to the mineralized bone tissues (Figure 12C). Finally, the ICP-OES analyses reveal that three oyster specimens are diagenetically unaltered and display concordant $^{87}Sr/^{86}Sr$ values as well as a similar Sr content (Figure 12D).
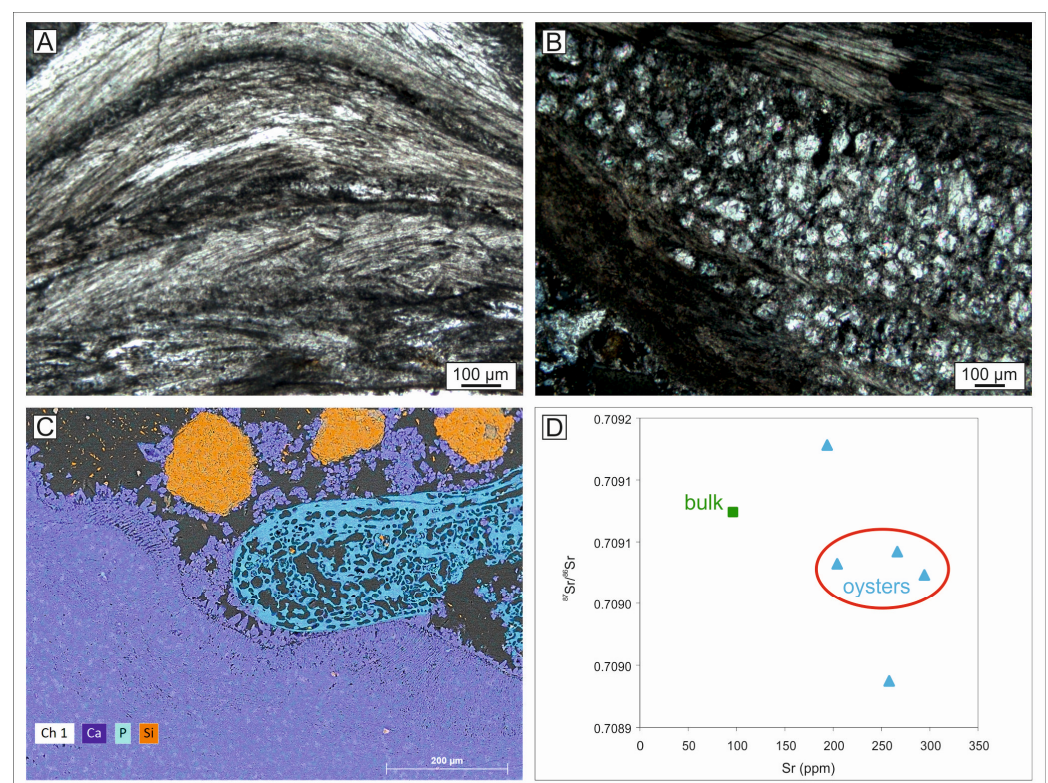
Figure 12. Diagenetic evaluation data for Strontium Isotope Stratigraphy. (**A**) Photomicrograph of the well-preserved prismatic layers of one of the analyzed oyster specimens (CA-OST2) under transmitted plane-polarized light. (**B**) Photomicrograph showing the alternation of prismatic and vesicular shell structures in one of the analyzed oyster specimens (CA-OST1) under transmitted cross-polarized light. (**C**) Compositional EDS map showing the Ca, P and Si distribution in the oyster sample CA-OST1. Note the oyster growing directly on the mineralized bone tissue (i.e., apatite). (**D**) Multi-component plot of $^{87}Sr/^{86}Sr$ vs. Sr concentration. The red ellipse indicates the concordant samples used for calculating the age of the fossil whale.

Sample CA-BULK6, i.e., the cemented sediment associated with oysters, exhibits high $^{87}Sr/^{86}Sr$ values and a low Sr content, and the same can be said for CA-OST3, which was discarded. Three oyster samples display consistent $^{87}Sr/^{86}Sr$ values and, as such, were used for calculating the final SIS age of the horizon in which the whale was found. The $^{87}Sr/^{86}Sr$ corrected values of CA-OST2, CA-OST4, and CA-OST5 are 0.709032, 0.709023, and 0.709042, respectively. Using the LOESS 6 curve calibrated on GTS2020 [75], the analyzed fossil oysters yield the preferred age values of 5.14 Ma, 5.40 Ma, and 4.79 Ma, respectively

(Table 3). Calculating a mean ^{87}Sr/^{86}Sr value for the fossil whale horizon, a mean preferred age of 5.11 Ma is obtained, with a maximum age of 5.59 Ma and a minimum age of 4.22 Ma (Table 2). These results strengthen the notion that the studied whale belongs to the Lower Pliocene Unit I and that its geological age was not younger than the middle Zanclean.

Table 3. Strontium isotope results reporting ^{87}Sr/^{86}Sr values, corrections based on the NIST NBS 987 and USGS EN-1 standards, and standard deviations, plus maximum ages, preferred ages, and minimum ages obtained from the LOESS 6 [75] for each analyzed sample. The mean of the selected ^{87}Sr/^{86}Sr values is calculated, showing the maximum age, the preferred age, and the minimum age of the fossil whale horizon.

Sample	Measured ^{87}Sr/^{86}Sr	Corrected ^{87}Sr/^{86}Sr	$\pm2\sigma_{mean}$	Max Age (Ma)	Preferred Age (Ma)	Min Age (Ma)
CA-OST1	0.708931	0.708937	0.000005	8.26	7.62	7.19
CA-OST2	**0.709026**	**0.709032**	**0.000004**	**5.38**	**5.14**	**4.86**
CA-OST3	0.709122	0.709128	0.000006	1.29	1.16	1.03
CA-OST4	**0.709017**	**0.709023**	**0.000005**	**5.61**	**5.40**	**5.13**
CA-OST5	**0.709036**	**0.709042**	**0.000005**	**5.11**	**4.79**	**4.01**
CA-BULK6	0.709068	0.709074	0.000005	2.68	2.37	2.10
Mean values of the horizon	**-**	**0.709033**	**0.000013**	**5.59**	**5.11**	**4.22**

5. Taphonomic History

5.1. Transport and Deposition

The ventral disposition of the Cádiz whale suggests that, after sinking to the seafloor for a first time, the cetacean carcass floated again to the surface before sinking definitively [8,18,25]. The floating of a whale is usually attributed to the formation and accumulation of putrefaction gases in the abdominal cavity during the decay process. Consequently, the whale carcasses can bloat, float, and ultimately flip ([8] and references therein). In the case of the studied whale, this hypothesis is supported by the observation of two disarticulated vertebrae as well as by the rotation of the thoracic portion of the vertebral column, which is usually either dorsally or ventrally disposed because the large body size prevents most whale carcasses from rolling [18]. However, at some time, the gases must have escaped, thus preventing a complete explosion of the rib cage [7], as the ribs are fully articulated. Another explanation for the rotation of the vertebral column involves a high-energy event at the seafloor that may have moved the whale skeleton laterally before its final burial. Unfortunately, it is not possible to reconstruct the original orientation of the carcass due to the detachment of the block from its original position.

The very high articulation degree (class 4) and the high completeness degree (at least class 3) suggest that the carcass did not undergo a significant dismembering after death and especially during refloating, which would have been limited in time and space. As suggested by Bosio et al. [18], dismemberment during floating may lead to a loss of completeness but not necessarily of articulation, which in turn can be lost for other reasons.

The Lower Pliocene depositional environment in which the whale sunk was a coastal, shallow-marine environment. That said, the skeletal assemblage of the layer in which the whale is preserved testifies to a deeper depositional environment compared to the overlying layers. The lowermost stratum (sample CA-PE2) is most likely related to a subtidal environment located below the wave base, possibly around ca. 50 to 60 m water depth, as also suggested by the abundance of planktic foraminifera and the presence of benthic foraminifera such as *Lenticulina* [97,98]. The middle stratum (sample CA-PE1) is probably related to a shallower setting, possibly less than 15 m water depth, given the presence of widespread *Thalassinoides* [99,100] and the high abundance of barnacle fragments [101]. *Thalassinoides*-bearing layers are often related to erosional or non-depositional discontinuities that usually correspond to sequence boundaries [102,103]. They typically result from periods of erosion or hiatuses in sedimentation during which an incipient lithification of the

sediment occurs, thus allowing the infaunal macroinvertebrates to burrow into a loose, fine-grained sediment that otherwise would have been too soft to serve as a substrate for such structures. When deposition starts again, all the burrows are filled by sediment [102,103]. The latter most likely deposited in a shallow-water setting at a few meters of water depth.

Given its skeletal assemblage, the uppermost stratum (sample CA-PE3) is probably related to a shallow-water setting, most likely less than 15 m deep [104,105]. The abundance of barnacles, mollusks, and bryozoans in the middle and upper strata also suggests a high nutrient supply, supporting a high primary productivity to sustain an abundant community of heterotrophs [104,106,107]. This interpretation is consistent with those proposed for other Pliocene deposits of Spain characterized by a similar skeletal assemblage [108–110]. The overall abundant presence of micrite and bioturbations and the lack of cross-lamination suggest a relatively protected setting with limited hydrodynamic energy. Overall, such a hypothetical paleoenvironmental setting is consistent with that proposed by other authors for the same deposits [67,111].

5.2. Permanence on the Seafloor

The degree of bone preservation and the associated faunal assemblage indicate that the Cádiz whale remained exposed for a long time on the seafloor before finally being buried. The low degree of bone cortical preservation, the occurrence of shark tooth marks, the fossil traces assigned to *Osedax*, and the microscopic evidence of abrasion, dissolution, and bioerosion of the compact bone tissue, together with the presence of encrusting organisms that grew up to large body size values, suggest a prolonged exposition of the defleshed skeleton on the seafloor.

A whale carcass on the seafloor constitutes a remarkable organic- and sulfide-rich habitat island. According to the "whale-fall community" approach, a whale carcass usually passes through four phases: (i) the mobile-scavenger stage, (ii) the enrichment-opportunist stage, (iii) the sulfophilic stage, and (iv) the reef stage [11].

In the first stage, which can last months (up to five years), soft tissue is removed from the carcass by aggregations of active necrophages. In our case, the discovery of as few as two shark tooth marks on a whale rib as well as of a couple of shark teeth in the close vicinity of the whale skeleton are suggestive of a scavenging action rather than of an active shark attack (e.g., [17,112–114]). These necrophagous actions operated by sharks such as *Carcharhinus* cf. *leucas* could contribute substantially to deflesh the carcass in a short time. Other animals with soft bodies could have also taken part in scavenging without getting preserved in the fossil record.

The second phase, the enrichment-opportunist stage, is here represented by pockmarks that have been attributed herein to *Osedax*. Such pockmarks have only been reported for two ribs, but recent erosion may have cancelled similar traces elsewhere. The enrichment-opportunist stage may take a few months up to two years, during which dense assemblages of heterotrophic macroinvertebrates, especially polychaetes and crustaceans, colonize the bones and the organically enriched sediments surrounding the carcass [11]. *Osedax* is a marine siboglinid annelid genus that has developed a unique metazoan–bacteria symbiosis to convert the organic material sequestered within the bones of dead vertebrates into an energy source [115], hence its vernacular name, "zombie worm". The posterior part of the zombie worm body penetrates into the bone tissue and features a root-like structure. The root absorbs collagen and lipids from the surrounding bone, whereas the gills extend into the surrounding seawater [54]. Fossil traces of *Osedax* are commonly found on fossil bones of whales and other marine vertebrates starting from the Cretaceous (e.g., [54,84–88]). *Osedax* bioerosion can lead to the complete destruction of whale skeletons [4,84]. In our case, the whale skeleton was likely only partially colonized by these worms.

The sulfophilic stage is somewhat underrepresented in our case study. During this phase, which may or may not occur and last up to 50 years, a chemolithoautotroph fauna colonizes the bones and surrounding sediments due to the production of sulfide from the anaerobic bacterial activity during the decomposition of bone lipids [11]. No sulphophilic

bivalves, such as the genera *Adipicola*, *Calyptogena*, *Conchocele*, *Idas*, *Solemya*, and *Vesicomya*, have been found at the site. However, microborings of the type B sensu Gariboldi et al. [94] and Bosio et al. [18] are found in thin sections of the bone tissue. Features such as the microboring infill of apatite enriched in Fe and framboidal Fe oxides associated with the bones suggest that their production is related to a sulfate-reducing bacterial activity responsible for the decay of the organic matter [10,18,94,95]. In addition, the presence of opaque minerals lining the dissolved external bone tissue evokes the occurrence of bacterial mats locally coating the bone surface. During lab-based experiments documenting the formation of framboidal iron sulfide growth on decaying vertebrate material in simulated marine settings, many framboids were indeed found on the bones, encapsulated in a biofilm associated with bone-covering bacterial mats [116]. This bacterial activity may reflect the sulfophilic stage of the Cádiz whale fall. The pyrite framboids may also have formed during this stage.

Evidence for the final pre-burial stage, i.e., the reef stage, is actually abundant. This stage is represented by suspension feeders colonizing the mineral parts and exploiting flow enhancement and hard substrates after the decomposition of organic matter [11]. Encrustation by balanid barnacles and bivalves such as ostreids indicate that the bones were bare before burial. Moreover, the fairly large dimensions reached by both the barnacle and the bivalve shells suggest a prolonged period of exposition of the defleshed bones on the seafloor. Balanid barnacle growth rates have been reported as ranging from 0.83 to 1.17 mm/day for the shell [117] or, more recently, from 1.0 to 1.5 ± 0.1 mm^2/day for the basal area [118]. Therefore, for reaching ca. 4 cm of height, at least ca. 40 days (and likely many more) should have passed from the settling of the larvae on bones.

After a long exposition on the seafloor, probably lasting months (but not more than a few years because the skeleton was still relatively intact; [119]), the whale was eventually buried and the subsequent fossilization processes could start.

5.3. Diagenesis and Mineralization

Macroscopically, bones can acquire a reddish color due to their impregnation by Fe hydroxides. The reddish color can be also observed microscopically through thin sections. In the Cádiz whale, the pinkish color can be ascribed to the locally abundant presence of Fe oxides in the bone cavities and within the bone microstructure.

For understanding the modes and timing of precipitation, it is important to focus on the distribution of Fe oxides. Pfretzschner [90,91] described different mechanisms for the formation of pyrite and iron oxides in fossil bones during diagenesis. In our case, framboidal pyrite precipitated during the very early stages of diagenesis. Fe oxide framboids are found in microborings and along the sediment–bone interface, probably as a result of the oxidation of primary precipitated pyrite. Pyrite precipitation in bones can be produced by two main mechanisms during two different stages of diagenesis: pyrite formation by sulfide precipitation in early diagenesis and pyrite formation by pH-dependent precipitation in late diagenesis [90]. In the first case, the one that is relevant to the Cádiz whale, pyrite precipitated in the very first phase of diagenesis, when microbial activity rather than environmental factors was the main influence on the chemical conditions within the bone. In fact, during organic decomposition, the reducing conditions and high organic matter content caused by the presence of the carcass itself could activate a process of Fe and sulphate reduction [120]. Laboratory experiments indicate that once the bones are defleshed by scavengers, pyrite framboids can precipitate within weeks of exposure [116].

On the other hand, in some cases, Fe oxides fill the osteocyte lacunae, canaliculi, and partially the Haversian canals and microcracks; furthermore, the edge of the osteons is characterized by a dark red color as the bone tissue has been substituted by Fe oxides. This case, i.e., the presence of pervasive Fe oxides that do not completely fill the Haversian canals, was interpreted by Pfretzschner [91] in terms of pH-dependent hematite precipitation during late diagenesis. Fe oxide formation by pH-dependent precipitation seems to have been rapid and restricted to the latest phases of apatite recrystallization,

when the microcracks formed due to the loss of collagen, but before the closure of the lacunae and canaliculi [91]. Finally, the bone apatite recrystallized, preserving all its histological features.

The hardness of a fossil bone can be related to the mineralization degree, which in turn depends on the processes that occurred during fossilization [10]. The moderate hardness of bones from the Cádiz whale is consistent with the aforementioned microscopic observations. The BSE images show poorly mineralized and fragile areas but also highly mineralized and Fe-enriched portions, especially where the pyrite framboids are concentrated. Moreover, several Haversian canals are filled by secondary calcite cement, which contributed to the hardness and permineralization of the fossil bones. Carbonates can precipitate in the early stages of diagenesis but usually retain evidence of this early precipitation (e.g., micro- and cryptocrystalline texture adhering to bone tissue, see [94]). In the Cádiz whale, the calcite cement is only present locally and displays a mosaic texture that typically indicates a late precipitation from Ca-enriched diagenetic fluids. During late diagenesis, secondary minerals such as sparry calcite can precipitate and fill the bone cavities, thus increasing the hardness of the fossil bone [10].

In conclusion, an early mineralization is pivotal for preserving vertebrates in the fossil record [120]. Early pyrite precipitation occurred within a few weeks of exposure, before burial. Ca phosphate mineral recrystallization should have followed swiftly even during the syn-burial stage, thanks to P availability due to phosphate liberation from the water column through sulfate reduction and the lowering of pH induced by the first products of organic matter decay [121,122]. During the late phases of recrystallization, Fe oxides started to precipitate, filling the bone cavities and permeating the bone tissue. After burial, bones experienced bioturbation by crustaceans that excavated the consolidated sediment to eventually reach the whale-embedding layer before the final cementation could take place. Finally, during late diagenesis, a calcite cement precipitated from circulating Ca-enriched fluids to fill several of the remaining empty cavities, thus further mineralizing the bone.

6. Conclusions

A fossil balaenopteroid whale was discovered at the locality of Conil de la Frontera (Cádiz, Spain) resting on an upside-down block detached from the nearby coastal cliff, where a Pliocene to Pleistocene sedimentary succession is exposed. ^{87}Sr/^{86}Sr analyses on three fossil oysters give an Early Pliocene age for the layer in which the fossil whale occurs, which fits well with the age of the lowest unit exposed at this locality. During the Early Pliocene, the paleoenvironment was a shallow-marine coastal setting. Taphonomic observations allowed the reconstruction of the taphonomic history of this balaenopteroid, which passed through all the whale-fall community stages: the mobile-scavenger stage, the enrichment-opportunist stage, the sulfophilic stage, and the reef stage. After death, the whale refloated again on the sea surface, where it lost some of the bones of the forelimbs and then sank to the seafloor in a ventral disposition. It remained unburied for long enough to be subject to scavenging, macro- and microbioerosion and to serve as a substrate for encrusting organisms. After burial, diagenetic processes led to the early permineralization of the bone tissue and the precipitation of secondary calcite cements, which contributed to the eventual preservation of the whale skeleton.

Supplementary Materials: The following supporting information can be downloaded at https://doi.org/10.6084/m9.figshare.24518479 (posted on 20 December 2023): 3D reconstruction of the fossil whale.

References

1. Peters, S.E.; Antar, M.S.M.; Zalmout, I.S.; Gingerich, P.D. Sequence stratigraphic control on preservation of late Eocene whales and other vertebrates at Wadi Al-Hitan, Egypt. *Palaios* **2009**, *24*, 290–302. [CrossRef]
2. Pyenson, N.D. The high fidelity of the cetacean stranding record: Insights into measuring diversity by integrating taphonomy and macroecology. *Proc. R. Soc. B Biol. Sci.* **2011**, *278*, 3608–3616. [CrossRef] [PubMed]
3. Hart, M.B. Geodiversity, palaeodiversity or biodiversity: Where is the place of palaeobiology and an understanding of taphonomy? *Proc. Geol. Assoc.* **2012**, *123*, 551–555. [CrossRef]
4. Dominici, S.; Danise, S.; Cau, S.; Freschi, A. The awkward record of fossil whales. *Earth-Sci. Rev.* **2020**, *205*, 103057. [CrossRef]
5. Bisconti, M.; Pellegrino, L.; Carnevale, G. The chronology of mysticete diversification (*Mammalia, Cetacea, Mysticeti*): Body size, morphological evolution and global change. *Earth-Sci. Rev.* **2023**, *239*, 104373. [CrossRef]
6. Schäfer, W. *Ecology and Palaeoecology of Marine Environments*; Chicago University Press: Chicago, IL, USA, 1972.
7. Reisdorf, A.G.; Bux, R.; Wyler, D.; Benecke, M.; Klug, C.; Maisch, M.W.; Fornaro, P.; Wetzel, A. Float, explode or sink: Postmortem fate of lung-breathing marine vertebrates. *Palaeobiodiv. Palaeoenviron.* **2012**, *92*, 67–81. [CrossRef]
8. Moore, M.J.; Mitchell, G.H.; Rowles, T.K.; Early, G. Dead cetacean? Beach, bloat, float, sink. *Front. Mar. Sci.* **2020**, *7*, 333. [CrossRef]
9. Gioncada, A.; Gariboldi, K.; Collareta, A.; Di Celma, C.; Bosio, G.; Malinverno, E.; Lambert, O.; Pike, J.; Urbina, M.; Bianucci, G. Looking for the key to preservation of fossil marine vertebrates in the Pisco Formation of Peru: New insights from a small dolphin skeleton. *Andean Geol.* **2018**, *45*, 379–398. [CrossRef]
10. Bosio, G.; Gioncada, A.; Gariboldi, K.; Bonaccorsi, E.; Collareta, A.; Pasero, M.; Di Celma, C.; Malinverno, E.; Urbina, M.; Bianucci, G. Mineralogical and geochemical characterization of fossil bones from a Miocene marine Konservat-Lagerstätte. *J. S. Am. Earth Sci.* **2021**, *105*, 102924. [CrossRef]
11. Smith, C.R.; Glover, A.G.; Treude, T.; Higgs, N.D.; Amon, D.J. Whale-fall ecosystems: Recent insights into ecology, paleoecology, and evolution. *Ann. Rev. Mar. Sc.* **2015**, *7*, 571–596. [CrossRef]
12. Allison, P.A.; Smith, C.R.; Kukert, H.; Deming, J.W.; Bennett, B.A. Deep-water taphonomy of vertebrate carcasses: A whale skeleton in the bathyal Santa Catalina Basin. *Paleobiology* **1991**, *17*, 78–89. [CrossRef]
13. Shapiro, R.S.; Spangler, E. Bacterial fossil record in whale-falls: Petrographic evidence of microbial sulfate reduction. *Palaeogeogr. Palaeoclim.* **2009**, *274*, 196–203. [CrossRef]
14. Danise, S.; Cavalazzi, B.; Dominici, S.; Westall, F.; Monechi, S.; Guioli, S. Evidence of microbial activity from a shallow water whale fall (Voghera, northern Italy). *Palaeogeogr. Palaeoclimatol. Palaeoecol.* **2012**, *317*, 13–26. [CrossRef]
15. Boessenecker, R.W.; Perry, F.A.; Schmitt, J.G. Comparative taphonomy, taphofacies, and bonebeds of the Mio-Pliocene Purisima Formation, Central California: Strong physical control on marine vertebrate preservation in shallow marine settings. *PLoS ONE* **2014**, *9*, e91419. [CrossRef] [PubMed]
16. Cuitiño, J.I.; Buono, M.R.; Viglino, M.; Farroni, N.D.; Bessone, S. Factors affecting the preservation and distribution of cetaceans in the lower Miocene Gaiman Formation of Patagonia, Argentina. *Palaeogeogr. Palaeoclimatol. Palaeoecol.* **2019**, *526*, 110–125. [CrossRef]

17. Tucker, J.P.; Vercoe, B.; Santos, I.R.; Dujmovic, M.; Butcher, P.A. Whale carcass scavenging by sharks. *Glob. Ecol. Conserv.* **2019**, *19*, e00655. [CrossRef]

18. Bosio, G.; Collareta, A.; Di Celma, C.; Lambert, O.; Marx, F.G.; de Muizon, C.; Gioncada, A.; Gariboldi, K.; Malinverno, E.; Varas-Malca, R.; et al. Taphonomy of marine vertebrates of the Pisco Formation (Miocene, Peru): Insights into the origin of an outstanding Fossil-Lagerstätte. *PLoS ONE* **2021**, *16*, e0254395. [CrossRef] [PubMed]

19. Bianucci, G. A new record of baleen whale from the Pliocene of Tuscany (Italy). *Atti. Soc. Tosc. Sci. Nat. Mem. Serie A* **1995**, *102*, 101–104.

20. Esperante, R.; Guinea, F.M.; Nick, K.E. Taphonomy of a Mysticeti whale in the Lower Pliocene Huelva Sands Formation (Southern Spain). *Geol. Acta* **2009**, *7*, 489–505.

21. Zazzera, A.; Girone, A.; La Perna, R.; Marino, M.; Maiorano, P.; Sardella, R.; Montenegro, V.; Francescangeli, R.; Bianucci, G. Systematics, taphonomy and palaeobiogeography of a balaenopterid (*Cetacea*, *Mysticeti*) from the Early Pleistocene of southern Italy. *Geobios* **2022**, *71*, 51–65. [CrossRef]

22. Bisconti, M.; Chicchi, S.; Monegatti, P.; Scacchetti, M.; Campanini, R.; Marsili, S.; Carnevale, G. Taphonomy, osteology and functional morphologyof a partially articulated skeleton of an archaic Pliocene right whale from Emilia Romagna (NW Italy). *Boll. Soc. Paleontol. Ital.* **2023**, *62*, 1–32.

23. Esperante, R.; Brand, L.R.; Chadwick, A.; Poma, O. Taphonomy of fossil whales in the diatomaceous sediments of the Miocene/Pliocene Pisco Formation, Peru. In *Current Topics on Taphonomy and Fossilization*; De Renzi, M., Pardo Alonso, M.V., Belinchón, M., Peñalver, E., Montoya, P., Márquez-Aliaga, A., Eds.; Ayuntamiento de Valencia: Valencia, Spain, 2002; pp. 337–343.

24. Danise, S.; Dominici, S. A record of fossil shallow-water whale falls from Italy. *Lethaia* **2014**, *47*, 229–243. [CrossRef]

25. Esperante, R.; Brand, L.R.; Chadwick, A.V.; Poma, O. Taphonomy and paleoenvironmental conditions of deposition of fossil whales in the diatomaceous sediments of the Miocene/Pliocene Pisco Formation, southern Peru—A new fossil-lagerstätte. *Palaeogeogr. Palaeoclimatol. Palaeoecol.* **2015**, *417*, 337–370. [CrossRef]

26. Bianucci, G.; Collareta, A.; Bosio, G.; Landini, W.; Gariboldi, K.; Gioncada, A.; Lambert, O.; Malinverno, E.; de Muizon, C.; Varas-Malca, R.; et al. Taphonomy and palaeoecology of the lower Miocene marine vertebrate assemblage of Ullujaya (Chilcatay Formation, East Pisco Basin, Southern Peru). *Palaeogeogr. Palaeoclimatol. Palaeoecol.* **2018**, *511*, 256–279. [CrossRef]

27. Bisconti, M.; Damarco, P.; Santagati, P.; Pavia, M.; Carnevale, G. Taphonomic patterns in the fossil record of baleen whales from the Pliocene of Piedmont, north-west Italy (*Mammalia, Cetacea, Mysticeti*). *Boll. Soc. Paleontol. Ital.* **2021**, *60*, 183–211.

28. Farroni, N.D.; Cuitiño, J.I.; Pérez, D.E.; Buono, M.R. Sedimentological and stratigraphically controlled preservation styles and distribution of fossil cetaceans from a new Early Miocene fossiliferous locality, Patagonia, Argentina. *Hist. Biol.* **2023**, 1–15. [CrossRef]

29. Pilleri, G. *Contributions to the Paleontology of Some Tethyan Cetacea and Sirenia: Record of Eurhinodelphis sp. (Cetacea: Rhabdosteidae) from the Lower Miocene of Catalonia, Spain*; Brain Anatomy Institute: Bern, Switzerland, 1988.

30. Pilleri, G.; Biosca, L.; Via, L. *The Tertiary Sirenia of Catalonia*; Brain Anatomy Institute: Bern, Switzerland, 1989.

31. Mendiola, C. Hallazgo de *Carcharodon carcharias* (Linnaeus 1758) en el Plioceno superior de Conil de la Frontera (Cádiz, Spain). *Rev. Soc. Paleontol. D'Elx* **2001**, *7*, 1–9.

32. Sendra, J.; Bajo, I. *Scaldicetus degiorgii* Varola, Landini & Pilleri,1988 (*Mammalia, Cetacea, Scaldicetidae*) del Mioceno (Tortoniense) de la Cuenca del Guadalquivir. In *XXIX Jornadas de Paleontología. Libro de Resúmenes*; Álvarez-Vázquez, C., Ed.; Córdoba, Spain, 2013. Available online: https://www.researchgate.net/publication/257237909_Scaldicetus_degiorgii_Varola_Landini_y_Pilleri_1988 _Mammalia_Cetacea_Scaldicetidae_del_Mioceno_Tortoniense_de_la_Cuenca_del_Guadalquivir (accessed on 17 December 2023).

33. Reolid, M.; Molina, J.M. Registro de *Carcharocles megalodon* en el sector oriental de la Cuenca del Guadalquivir (Mioceno superior, Sur de España). *Estud. Geol.* **2015**, *71*, e032. [CrossRef]

34. Reolid, M.; García-García, F.; Reolid, J.; De Castro, A.; Bueno, J.F.; Martín-Suárez, E. Palaeoenvironmental interpretation of a sand-dominated coastal system of the Upper Miocene of eastern Guadalquivir Basin (South Spain): Fossil assemblages, ichnology and taphonomy. *J. Iber. Geol.* **2016**, *42*, 275–290. [CrossRef]

35. Sendra, J. Los yacimientos de mamíferos marinos del Neógeno del Surde la provincia de Alicante. In *Resúmenes XIII Jornadas de Paleontología*; Grandal D'Anglade, A., Gutiérrez-Marco, J.C., Santos Fidalgo, L., Eds.; Sociedad Española de Paleontología: La Coruña, Spain, 1997; pp. 237–240.

36. Mercadal, B.; Pilleri, G.; Casinos, A. A tooth of *Scaldicetus grandis* (Du Bus, 1872) (Physeteridae) from Aire Island (Menorca, Spain). *Investig. Cetacea* **1985**, *17*, 31–33.

37. Pilleri, G. Miocene cetacean remains from Mediterranean Spain. *Treb. Del Mus. Geol. Barc.* **1990**, *1*, 43–76.

38. Miján, I. Hallazgos de restos fósiles de *Hyperoodon* sp. (*Cetacea, Ziphiidae*) en las costas gallegas (NO España). *Rev. Biol. Mar. Oceanogr.* **2007**, *42*, 253–260. [CrossRef]

39. Bianucci, G.; Miján, I.; Lambert, O.; Post, K.; Mateus, O. Bizarre fossil beaked whales (*Odontoceti, Ziphiidae*) fished from the Atlantic Ocean floor off the Iberian Peninsula. *Geodiversitas* **2013**, *35*, 105–153. [CrossRef]

40. Bianucci, G.; Llàcer, S.; Cardona, J.Q.; Collareta, A.; Florit, A.R. A new beaked whale record from the upper Miocene of Menorca, Balearic Islands, based on CT-scan analysis of limestone slabs. *Acta Palaeontol. Pol.* **2019**, *64*, 291–302. [CrossRef]

41. Mas, G.; Escalante, F.; Quintana, J. Primera cita de un Delphinidae en el Neógeno de las Islas Baleares. *Batalleria* **2013**, *18*, 45–51.

42. Toscano, A.; Abad, M.; Ruiz, F.; Muñiz, F.; Álvarez, G.; García, E.X.M.; Caro, J.A. Nuevos restos de *Scaldicetus* (*Cetacea, Odontoceti, Physeteridae*) del Mioceno superior, sector occidental de la Cuenca del Guadalquivir (sur de España). *Rev. Mex. Cienc. Geol.* **2013**, *30*, 436–445.

43. Miján, I.; Louwye, S.; Lambert, O. A new *Beneziphius* beaked whale from the ocean floor off Galicia, Spain and biostratigraphic reassessment of the type species. *Acta Palaeont. Pol.* **2017**, *62*, 211–220. [CrossRef]

44. Sendra, S.J.; Hodgson, D. *Astadelphis gastaldii* (Brandt, 1874)-Mammalia, Cetacea, Delphinidae-en el Plioceno Espanol. *Libro Resúmenes XIV J. Paleontol.* **1998**, *14*, 169–172.

45. López Amador, J.J.; Ruiz Gil, J.A. Patrimonio natural de la Bahía de Cádiz: El yacimiento terciario de El Manatial. *Rev. Atlánt.-Mediterr. Prehist. Arqueol. Soc.* **2016**, *18*, 163–169. [CrossRef]

46. Sendra, J.; Reolid, M.; Reolid, J. Palaeoenvironmental interpretation of the Pliocene fan-delta system of the Vera Basin (SE Spain): Fossil assemblages, ichnology and taphonomy. *Palaeoworld* **2020**, *29*, 769–788. [CrossRef]

47. Belaústegui, Z.; de Gibert, J.M.; Domènech, R.; Muñiz, F.; Martinell, J. Tafonomía y contexto paleoambiental de los restos de un cetáceo del Mioceno medio de Tarragona (NE España). *Geobios* **2011**, *44*, 19–31. [CrossRef]

48. Belaústegui, Z.; de Gibert, J.M.; Domènech, R.; Muñiz, F.; Martinell, J. Clavate borings in a Miocene cetacean skeleton from Tarragona (NE Spain) and the fossil record of marine bone bioerosion. *Palaeogeogr. Palaeoclimatol. Palaeoecol.* **2012**, *323*, 68–74. [CrossRef]

49. Sendra, J.; Bajo Campos, I. Evidencias tafonómicas de carroñeo o predación sobre cetáceos: El neurocráneo del Tortoniense de Burguillos (Sevilla). In Proceedings of the XXIX Jornadas de Paleontología de la Sociedad Española de Paleontología, Córdoba, Spain, 2–5 October 2013.

50. Sendra, J.; Bajo, I.; Cardenas, J. Un ejemplar de Misticeto (*Mammalia*: *Cetacea*) del Plioceno inferior de Alcalá de Guadaira (Sevilla). *J. Paleontol.* **1996**, *12*, 116–117.

51. Sendra, J.; Stokes, M.; Oltra, V. Excavación de un misticeto (Mammalia, Cetacea) en el Plioceno del sector norte de la Cuenca Vera (Almería). In Proceedings of the XIV Jornadas de Paleontología, Sociedad Española de Paleontología, Tenerife, Spain, 7–11 October 1998.

52. Sendra, J.; Muñiz, F.; Mayoral, E. Primeros datos sobre misticetos (*Mammalia*, *Cetacea*, *Balaenopteridae*) en el Plioceno Inferior de la Cuencadel Guadalquivir (Lepe, Huelva). *Temas Geológico-Min.* **1999**, *26*, 356–361.

53. Sendra, J.; Muñiz, F.; Mayoral, E.; De Renzi, M. Nuevos datos sobre Misticetos (*Mammalia*, *Cetacea*) en el Plioceno Inferior de La Cuenca del Guadalquivir (Lepe, Huelva, España). In Proceedings of the Libro de Resúmenes del I Congreso Ibérico de Paleontología y XVI Jornadas de La Sociedad Española de Paleontología, Spain, 12–14 October 2000.

54. Muñiz, F.; De Gibert, J.M.; Esperante, R. First trace-fossil evidence of bone-eating worms in whale carcasses. *Palaios* **2010**, *25*, 269–273. [CrossRef]

55. Mayoral, E.; Muñiz, F.; Sendra, J.; Bajo, I.; Cárdenas, J. Prospección paleontológica superficial en las márgenes del Río Guadaira, en el término municipal de Alcalá de Guadaira (Sevilla). *Anu. Arqueol. Andal.* **2001**, *97*, 1651–1659.

56. Mayoral, E.; Muñiz, F.; Sendra, J. Sondeo estratigráfico de urgencia enel Cabezo del Tío Parra, Lepe (Huelva). *Anu. Arqueol. Andal.* **2001**, *97*, 370–374.

57. Berástegui, X.; Banks, C.J.; Puig, C.; Taberner, C.; Waltham, D.; Fernández, M. Lateral diapiric emplacement of Triassic evaporites at the southern margin of the Guadalquivir Basin, Spain. *Geol. Soc. Spec. Publ.* **1998**, *134*, 49–68. [CrossRef]

58. Garcia-Castellanos, D.; Fernandez, M.; Torné, M. Modeling the evolution of the Guadalquivir foreland basin (Southern Spain). *Tectonics* **2002**, *21*, 1–17. [CrossRef]

59. Braga, J.C.; Martín, J.M.; Riding, R.; Aguirre, J.; Sánchez-Almazo, I.M.; Dinarès-Turell, J. Testing models for the Messinian salinity crisis: The Messinian record in Almería, SE Spain. *Sediment. Geol.* **2006**, *188*, 131–154. [CrossRef]

60. Martín, J.M.; Braga, J.C.; Aguirre, J.; Puga-Bernabéu, Á. History and evolution of the North-Betic Strait (Prebetic Zone, Betic Cordillera): A narrow, early Tortonian, tidal-dominated, Atlantic–Mediterranean marine passage. *Sediment. Geol.* **2009**, *216*, 80–90. [CrossRef]

61. Krijgsman, W.; Capella, W.; Simon, D.; Hilgen, F.J.; Kouwenhoven, T.J.; Meijer, P.T.; Sierro, F.J.; Tulbure, M.A.; van den Berg, B.C.J.; van der Schee, M.; et al. The Gibraltar corridor: Watergate of the Messinian salinity crisis. *Mar. Geol.* **2018**, *403*, 238–246. [CrossRef]

62. Reolid, J.; Aguirre, J.; Pérez-Asensio, J.N.; Puga-Bernabéu, Á.; Braga, J.C.; Martín, J.M. Mixed carbonate-siliciclastic contourite drift deposits associated with the entrance of an Atlantic-Mediterranean corridor (Late Miocene, Southwest Spain). *Sediment. Geol.* **2022**, *439*, 106233. [CrossRef]

63. Rouchy, J.M.; Caruso, A. The Messinian salinity crisis in the Mediterranean basin: A reassessment of the data and an integrated scenario. *Sediment. Geol.* **2006**, *188*, 35–67. [CrossRef]

64. Viguier, C. Le Néogéne de l'Andalousie Nord-Occidental (Espagne). Histoire Géologique du bas Guadalquivir. Ph.D. Thesis, Thése Bordeaux, Burdeos, France, 1974; p. 449.

65. Aguirre, J. Implicaciones paleoambientales y paleogeográficas de dos discontinuidades estratigráficas en los depósitos pliocénicos de Cádiz (SW de España). *Rev. Soc. Geol. España* **1995**, *8*, 153–166.

66. Droser, M.L.; Bottjer, D.J. Ichnofabric of sandstones deposited in high-energy nearshore environments: Measurement and utilization. *Palaios* **1989**, *4*, 598–604. [CrossRef]

67. Aguirre, J.; De Gibert, J.M.; Puga-Bernabéu, A. Proximal–distal ichnofabric changes in a siliciclastic shelf, Early Pliocene, Guadalquivir Basin, southwest Spain. *Palaeogeogr. Palaeocl.* **2010**, *291*, 328–337. [CrossRef]

68. Aguirre Rodriguez, J. Estratigrafía del Plioceno de la costa de Cádiz entre Chiclana y Conil. *Geogaceta* **1991**, *9*, 84–87.

69. Gutiérrez-Mas, J.M.; Mas, R. Record of very high energy events in Plio-Pleistocene marine deposits of the Gulf of Cadiz (SW Spain): Facies and processes. *Facies* **2013**, *59*, 679–701. [CrossRef]

70. Yoshida, H.; Shirakihara, M.; Takemura, A.; Shirakihara, K. Development, sexual dimorphism, and individual variation in the skeleton of the finless porpoise, *Neophocaena phocaenoides*, in the coastal waters of western Kyushu, Japan. *Mar. Mamm. Sci.* **1994**, *10*, 266–282. [CrossRef]

71. Tsai, C.H. A Miocene breeding ground of an extinct baleen whale (*Cetacea*: *Mysticeti*). *PeerJ* **2017**, *5*, e3711. [CrossRef]

72. Baccelle, L.; Bosellini, A. *Diagrammi per la Stima Visiva Della Composizione Percentuale Nelle Rocce Sedimentary*; Nuova Serie, Sezione IX, Scienze Geologiche e Paleontologiche; Annali Università di Ferrara: Ferrara, Italy, 1965; pp. 59–89.

73. Flügel, E. *Microfacies of Carbonate Rocks: Analysis Interpretation and Application*; Springer: New York, NY, USA, 2010; p. 984.

74. Bosio, G.; Malinverno, E.; Collareta, A.; Di Celma, C.; Gioncada, A.; Parente, M.; Berra, F.; Marx, F.G.; Vertino, A.; Urbina, M.; et al. Strontium isotope stratigraphy and the thermophilic fossil fauna from the middle Miocene of the East Pisco Basin (Peru). *J. S. Am. Earth Sci.* **2020**, *97*, 102399. [CrossRef]

75. McArthur, J.M.; Howarth, R.J.; Shields, G.A.; Zhou, Y. Strontium isotope stratigraphy. In *Geologic Time Scale 2020*; Gradstein, F.M., Ogg, J.G., Schmitz, M.D., Ogg, G.M., Eds.; Elsevier: Amsterdam, The Netherlands, 2020; pp. 211–238.

76. Frijia, G.; Parente, M.; Di Lucia, M.; Mutti, M. Carbon and strontium isotope stratigraphy of the Upper Cretaceous (Cenomanian-Campanian) shallow-water carbonates of southern Italy: Chronostratigraphic calibration of larger foraminifera biostratigraphy. *Cretac. Res.* **2015**, *53*, 110–139. [CrossRef]

77. Bosio, G.; Bianucci, G.; Collareta, A.; Landini, W.; Urbina, M.; Di Celma, C. Ultrastructure, composition, and $^{87}Sr/^{86}Sr$ dating of shark teeth from lower Miocene sediments of southwestern Peru. *J. S. Am. Earth Sci.* **2022**, *118*, 103909. [CrossRef]

78. Lowe, D.G. Object recognition from local scale-invariant features. In Proceedings of the Seventh IEEE International Conference on Computer Vision, Kerkyra, Greece, 20–27 September 1999; Volume 2, pp. 1150–1157.

79. Carabassa, V.; Montero, P.; Crespo, M.; Padró, J.C.; Pons, X.; Balagué, J.; Brotons, L.; Alcañiz, J.M. Unmanned aerial system protocol for quarry restoration and mineral extraction monitoring. *J. Environ. Manag.* **2020**, *270*, 110717. [CrossRef] [PubMed]

80. Zonneveld, J.P.; Fiorillo, A.R.; Hasiotis, S.; Gingras, M.K. Tooth marks, gnaw marks, claw-marks, bite marks, scratch marks, etc.: Terminology in ichnology. *Ichnos* **2022**, *29*, 93–101. [CrossRef]

81. Cigala Fulgosi, F. Predation (or possible scavenging) by a great white shark on an extinct species of bottlenosed dolphin in the Italian Pliocene. *Tert. Res.* **1990**, *12*, 17–36.

82. Bianucci, G.; Sorce, B.; Storai, T.; Landini, W. Killing in the Pliocene: Shark attack on a dolphin from Italy. *Palaeontology* **2010**, *53*, 457–470. [CrossRef]

83. Collareta, A.; Lambert, O.; Landini, W.; Di Celma, C.; Malinverno, E.; Varas-Malca, R.; Urbina, M.; Bianucci, G. Did the giant extinct shark *Carcharocles megalodon* target small prey? Bite marks on marine mammal remains from the late Miocene of Peru. *Palaeogeogr. Palaeoclimatol. Palaeoecol.* **2017**, *469*, 84–91. [CrossRef]

84. Kiel, S.; Goedert, J.L.; Kahl, W.A.; Rouse, G.W. Fossil traces of the bone-eating worm *Osedax* in early Oligocene whale bones. *Proc. Natl. Acad. Sci. USA* **2010**, *107*, 8656–8659. [CrossRef]

85. Danise, S.; Higgs, N.D. Bone-eating *Osedax* worms lived on Mesozoic marine reptile deadfalls. *Biol. Lett.* **2015**, *11*, 20150072. [CrossRef] [PubMed]

86. Higgs, N.D.; Little, C.T.; Glover, A.G.; Dahlgren, T.G.; Smith, C.R.; Dominici, S. Evidence of *Osedax* worm borings in Pliocene (∼3 Ma) whale bone from the Mediterranean. *Hist. Biol.* **2012**, *24*, 269–277.

87. Higgs, N.D.; Pokines, J.T. Marine environmental alterations to bone. In *Manual of Forensic Taphonomy*; Pokines, J.T., Symes, S.A., Eds.; CRC Press: Boca Raton, FL, USA, 2013; pp. 143–179.

88. Boessenecker, R.W.; Fordyce, R.E. Trace fossil evidence of predation upon bone-eating worms on a baleen whale skeleton from the Oligocene of New Zealand. *Lethaia* **2015**, *48*, 326–331. [CrossRef]

89. Bloebaum, R.D.; Skedros, J.G.; Vajda, E.G.; Bachus, K.N.; Constantz, B.R. Determining mineral content variations in bone using backscattered electron imaging. *Bone* **1997**, *20*, 485–490. [CrossRef]

90. Pfretzschner, H.U. Pyrite in fossil bone. *N. Jb. Geol. Paläont. Abh.* **2001**, *220*, 1–23. [CrossRef]

91. Pfretzschner, H.U. Iron oxides in fossil bone. *N. Jb. Geol. Paläont. Abh.* **2001**, *220*, 417–429. [CrossRef]

92. Bodzioch, A. Idealized model of mineral infillings in bones of fossil freshwater animals, on the example of Late Triassic metoposaurs from Krasiejów (Poland). *Austin J. Earth Sci.* **2015**, *2*, 1008.

93. Pfretzschner, H.U. Microcracks and fossilization of Haversian bone. *N. Jb. Geol. Paläont. Abh.* **2000**, *216*, 413–432. [CrossRef]

94. Gariboldi, K.; Gioncada, A.; Bosio, G.; Malinverno, E.; Di Celma, C.; Tinelli, C.; Cantalamessa, G.; Landini, W.; Urbina, M.; Bianucci, G. The dolomite nodules enclosing fossil marine vertebrates in the East Pisco Basin, Peru: Field and petrographic insights into the Lagerstätte formation. *Palaeogeogr. Palaeoclimatol. Palaeoecol.* **2015**, *438*, 81–95. [CrossRef]

95. Jans, M.M.E. Microbial bioerosion of bone—A review. In *Current Developments in Bioerosion*; Wisshak, M., Tapanila, L., Eds.; Springer: Berlin/Heidelberg, Germany, 2008; pp. 397–413.

96. Cox, L.R.; Newell, N.D.; Boyd, D.W.; Branson, C.C.; Casey, R.; Chavan, A.; Coogan, A.H.; Dechaseaux, C.; Fleming, C.A.; Haas, F.; et al. Mollusca (Bivalvia). In *Treatise of Invertebrate Paleontology*; Moore, R.C., Ed.; The University of Kansas Printing Service: Lawrence, KS, USA; Meriden, CT, USA; New York, NY, USA, 1971; pp. N1–N1224.

97. Van der Zwaan, G.J.; Jorissen, F.J.; De Stigter, H.C. The depth dependency of planktonic/benthic foraminiferal ratios: Constraints and applications. *Mar. Geol.* **1990**, *95*, 1–16. [CrossRef]

98. Murray, J.W. *Ecology and Applications of Benthic Foraminifera*; Cambridge University Press: Cambridge, UK, 2006; p. 318.

99. Bromley, R.G.; Frey, R.W. Redescription of the trace fossil *Gyrolithes* and taxonomic evaluation of *Thalassinoides*, *Ophiomorpha* and *Spongeliomorpha*. *Bull. Geol. Soc. Den.* **1974**, *23*, 311–335.

100. Coleman, N.; Poore, G.C.B. The distribution of *Callianassa* species (*Crustacea*, *Decapoda*) in Western Port, Victoria. *Proc. R. Soc. Vic.* **1980**, *91*, 73–78.

101. Coletti, G.; Bosio, G.; Collareta, A.; Bialik, O.M.; Regattieri, E.; Cornacchia, I.; Buckeridge, J. Barnacle-rich facies as a tool for palaeoenvironmental reconstructions. *Palaeogeogr. Palaeoclimatol. Palaeoecol.* **2024**, *634*, 111914. [CrossRef]

102. MacEachern, J.A.; Raychaudhuri, I.; Pemberton, S.G. Stratigraphic applications of the *Glossifungites* ichnofacies: Delineating discontinuities in the rock record. In *Applications of Ichnology to Petroleum Exploration*; Pemberton, S.G., Ed.; Core Workshop Notes; SEPM Society for Sedimentary Geology: Tulsa, OK, USA, 1992; Volume 17, pp. 169–198.

103. Abdel-Fattah, Z.A.; Gingras, M.K.; Caldwell, M.W.; Pemberton, S.G.; MacEachern, J.A. The *Glossifungites* ichnofacies and sequence stratigraphic analysis: A case study from middle to upper Eocene successions in Fayum, Egypt. *Ichnos* **2016**, *23*, 157–179. [CrossRef]

104. Coletti, G.; Bosio, G.; Collareta, A.; Buckeridge, J.; Consani, S.; El Kateb, A. Palaeoenvironmental analysis of the Miocene barnacle facies: Case studies from Europe and South America. *Geol. Carpathica* **2018**, *69*, 573–592. [CrossRef]

105. Coletti, G.; Bosio, G.; Collareta, A. Lower Pliocene barnacle facies of western Liguria (NW Italy): A peek into a warm past and a glimpse of our incoming future. *Riv. Ital. Paleontol. Stratigr.* **2021**, *127*, 103–131.

106. Westphal, H.; Halfar, J.; Freiwald, A. Heterozoan carbonates in subtropical to tropical settings in the present and past. Int. *J. Earth Sci.* **2010**, *99*, 153–169.

107. Bialik, O.M.; Coletti, G.; Mariani, L.; Commissario, L.; Desbiolles, F.; Meroni, A.N. Availability and type of energy regulate the global distribution of neritic carbonates. *Sci. Rep.* **2023**, *13*, 19687. [CrossRef]

108. Martín, J.M.; Braga, J.C.; Aguirre, J.; Betzler, C. Contrasting models of temperate carbonate sedimentation in a small Mediterranean embayment: The Pliocene Carboneras Basin, SE Spain. *J. Geol. Soc.* **2004**, *161*, 387–399. [CrossRef]

109. Braga, J.C.; Martín, J.M.; Betzler, C.; Aguirre, J. Models of temperate carbonate deposition in Neogene basins in SE Spain: A synthesis. *Geol. Soc. Lond. Spec. Publ.* **2006**, *255*, 121–135. [CrossRef]

110. Aguirre, J.; Martín, J.M.; Braga, J.C.; Betzler, C.; Berning, B.; Buckeridge, J.S. Densely packed concentrations of sessile barnacles (*Cirripedia*: *Sessilia*) from the Early Pliocene of SE Spain. *Facies* **2008**, *54*, 193–206. [CrossRef]

111. Rico-García, A.; Aguirre, J.; González-Delgado, J.Á. Taphonomy and taphofacies models of the Pliocene deposits of Vejer de la Frontera (Cádiz, SW Spain). *Geobios* **2008**, *41*, 543–558. [CrossRef]

112. Curtis, T.H.; Kelly, J.T.; Menard, K.L.; Laroche, R.K.; Jones, R.E.; Klimley, A.P. Observations on the behavior of white sharks scavenging from a whale carcass at Point Reyes, California. *Calif Fish Game* **2006**, *92*, 113–124.

113. Fallows, C.; Gallagher, A.J.; Hammerschlag, N. White sharks (*Carcharodon carcharias*) scavenging on whales and its potential role in further shaping the ecology of an apex predator. *PLoS ONE* **2013**, *8*, e60797. [CrossRef] [PubMed]

114. Lea, J.S.E.; Daly, R.; Leon, C.; Daly, C.A.K.; Clarke, C.R. Life after death: Behaviour of multiple shark species scavenging a whale carcass. *Mar. Freshw. Res.* **2018**, *70*, 302–306. [CrossRef]

115. Goffredi, S.K.; Orphan, V.J.; Rouse, G.W.; Jahnke, L.; Embaye, T.; Turk, K.; Lee, R.; Vrijenhoek, R.C. Evolutionary innovation: A bone-eating marine symbiosis. *Environ. Microbiol.* **2005**, *7*, 1369–1378. [CrossRef] [PubMed]

116. Vietti, L.A.; Bailey, J.V.; Fox, D.L.; Rogers, R.R. Rapid formation of framboidal sulfides on bone surfaces from a simulated marine carcass fall. *Palaios* **2015**, *30*, 327–334. [CrossRef]

117. Crisp, D.J.; Bourget, E. Growth in barnacles. In *Advances in Marine Biology*; Academic Press: Cambridge, MA, USA, 1985; Volume 22, pp. 199–244.

118. Nishizaki, M.T.; Carrington, E. The effect of water temperature and velocity on barnacle growth: Quantifying the impact of multiple environmental stressors. *J. Therm. Biol.* **2015**, *54*, 37–46. [CrossRef]

119. Lundsten, L.; Schlining, K.L.; Frasier, K.; Johnson, S.B.; Kuhnz, L.A.; Harvey, J.B.; Clague, G.; Vrijenhoek, R.C. Time-series analysis of six whale-fall communities in Monterey Canyon, California, USA. *Deep Sea Res. Part I* **2010**, *57*, 1573–1584. [CrossRef]

120. Allison, P.A. The role of anoxia in the decay and mineralization of proteinaceous macro-fossils. *Paleobiology* **1988**, *14*, 139–154. [CrossRef]

121. Berna, F.; Matthews, A.; Weiner, S. Solubilities of bone mineral from archaeological sites: The recrystallization window. *J. Archaeol. Sci.* **2004**, *31*, 867–882. [CrossRef]

122. Creveling, J.R.; Johnston, D.T.; Poulton, S.W.; Kotrc, B.; März, C.; Schrag, D.P.; Knoll, A.H. Phosphorus sources for phosphatic Cambrian carbonates. *GSA Bull.* **2014**, *126*, 145–163. [CrossRef]